Revising inelastic dark matter direct detection by including the cosmic ray acceleration

Jie-Cheng Feng,[a] **Xian-Wei Kang,**[b,c,1] **Chih-Ting Lu,**[d] **Yue-Lin Sming Tsai**[e,1] **and Feng-Shou Zhang**[b,c]

[a]*Department of Physics, Beijing Normal University,*
Beijing 100875, China

[b]*Key Laboratory of Beam Technology of the Ministry of Education,*
College of Nuclear Science and Technology, Beijing Normal University,
Beijing 100875, China

[c]*Beijing Radiation Center,*
Beijing 100875, China

[d]*Department of Physics and Institute of Theoretical Physics, Nanjing Normal University,*
Nanjing, 210023, China

[e]*Key Laboratory of Dark Matter and Space Astronomy,*
Purple Mountain Observatory, Chinese Academy of Sciences,
Nanjing 210033, China

E-mail: 201811140244@mail.bnu.edu.cn, xwkang@bnu.edu.cn,
timluyu@kias.re.kr, smingtsai@pmo.ac.cn, fszhang@bnu.edu.cn

ABSTRACT: The null signal from collider and dark matter (DM) direct detector experiments makes the interaction between DM and visible matter too small to reproduce the correct relic density for many thermal DM models. The remaining parameter space indicates that two almost degenerated states in the dark sector, the inelastic DM scenario, can co-annihilate in the early universe to produce the correct relic density. Regarding the direct detection of the inelastic DM scenario, the virialized DM component from the nearby halo is nonrelativistic and not able to excite the DM ground state, even if the relevant couplings can be considerable. Thus, a DM with a large mass splitting can evade traditional virialized DM direct detection. In this study, we connect the concept of cosmic-ray accelerated DM in our Milky Way and the direct detection of inelastic scattering in underground detectors to explore spectra that result from several interaction types of the inelastic DM. We find that the mass splitting $\delta < \mathcal{O}(1\,\mathrm{GeV})$ can still be reachable for cosmic ray accelerated DM with mass range $1\,\mathrm{MeV} < m_{\chi_1} < 100\,\mathrm{GeV}$ and sub-GeV light mediator using the latest PandaX-4T data, even though we conservatively use the astrophysical parameter (effective length) $D_{\mathrm{eff}} = 1$ kpc.

[1]Corresponding author.

Contents

1 Introduction

The gravitational evidence of dark matter (DM) is strong and clear. However, its nongravitational interaction with the standard model (SM) has not yet been observed. Conversely, if the DM number density in the early universe can be described by the thermal Boltzmann distribution, such as the SM particles, the Planck measured relic density [1] implies that DM must interact with the SM besides gravity. Among the various methods to detect the interaction between DM and SM, laboratory measurements, including the Large Hadron Collider (LHC) [2, 3] and DM direct detection (DD) [4, 5], provide the most robust searches. However, only null signals have been reported. Particularly, the limits from either XENON1T [4] or PandaX-4T [5] rule out the DM-proton elastic scattering cross section close to the neutrino floor. These stringent constraints squeeze the allowed DM model
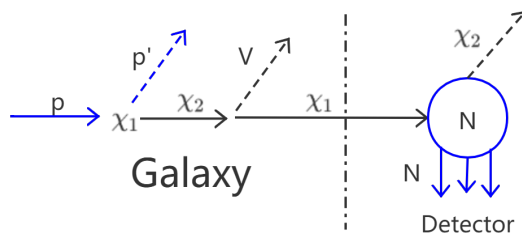
Figure 1. Cosmic ray accelerated inelastic DM detection scenario: $p + \chi_1 \to p' + \chi_2 \to p' + \chi_1 + V$, where p denotes the CR proton or helium, and the prime is used to distinguish the same particles in the initial and final states. The inelastic DM χ_1 and χ_2 are the ground state and excited state, respectively; V is the mediator between SM and DM; and N is the target nucleus inside the underground detector. By this mechanism, the final χ_1 is accelerated.

parameter space to some fine-tuning regions where the correct relic density is generated by some special mechanisms (e.g., resonance or coannihilation [6]). The coannihilation region indicates that the lightest DM particle χ_1 and the next lightest one χ_2 almost degenerate in mass. When the coannihilation mechanism governs DM annihilations, the $\chi_1 - \chi_1 -$SM coupling can be negligible. Thus, the $\chi_1 - p$ elastic scattering will be suppressed [7–12]. In contrast, the resonance region (the mass of the mediator such as Higgs equal to twice the DM mass) may be completely probed in future DD sensitivities (e.g., see Higgs portal DM models [13–18]).

The standard DM DD strategy is to detect DM-nucleon interactions by measuring the recoil energy of DM-nucleon scattering under the following consideration. When the Earth sweeps the local virialized halo, the Maxwell-Boltzmann distributed DM, hereafter called virialized DM (vDM), hits the detector target. Because the vDM velocity is non-relativistic, the currently measured nuclei recoil energy range does not cover DM mass lighter than $\approx 5\,\text{GeV}$ for xenon-type detectors [4, 5, 19]. Also, such a standard method may also be blind when searching the coannihilation region because the incoming vDM is non-relativistic and its small kinetic energy cannot excite DM to the next lightest one, namely its kinetic energy smaller than the mass difference between χ_1 to χ_2. Quantitatively, a DM mass heavier than $\mathcal{O}(\text{TeV})$ is needed to detect an excitation from χ_1 to χ_2 with the mass splitting $\approx \mathcal{O}(100\,\text{keV})$ [20].

Other researchers have proposed searching for accelerated vDMs by considering their collisions with the high energy cosmic ray (CR) protons [21–25]. When collisions occur, the DM mass below a few GeV can be accelerated to be relativistic and enter the underground detector with kinetic energy higher than the designed threshold energy. This kind of cosmic ray accelerated vDM (CRDM), has recently received much attention because it demonstrates what is possible to detect sub-GeV DM with current DM DD experiments. Even if CRDM fluxes are several orders of magnitude lower than those of vDM, the detection of CRDM helps us to probe the DM mass region lighter than a few GeV using the sensitivity of XENONnT and PandaX-4T. This DM mass region was almost undetectable by using the vDM scenario. With a similar idea, light CRDM can be detected with a

neutrino telescope [26] or by studying the diurnal effect caused by light CRDM [27]. In addition, such a collision between the CR proton and DM may also smash the proton and produce neutrino and gamma ray [28].

We extend the CRDM elastic scattering to the inelastic scattering scenario (see the schematic carton in figure 1). The first vertex occurs in the Milky Way, where χ_1 is excited to χ_2 after the first collision. Unlike the elastic CRDM scenario, χ_2 is not a stable particle and subsequently decays back to χ_1 and emits a mediator particle V before reaching the underground detector. The velocity of χ_1 here can be higher than elastic CRDM because the decay from heavier χ_2 can boost χ_1 again. Recently, investigating a similar scenario with the vector-vector interaction between femionic DM and SM, ref. [29] found that this approach can probe a larger mass splitting $\approx 100\,\mathrm{MeV}$. Conversely, the traditional vDM inelastic scattering search is limited to the heavier mass and low mass splitting [20].

In this study, we consider both elastically and inelastically produced CRDM. To clarify their difference, we list their productions and mass splitting δ conditions as follows:

- For inelastic scattering, the full process is $p + \chi_1 \to p' + \chi_2 \to p' + \chi_1 + V$ as shown in figure 1, where the mass splitting δ between χ_1 and χ_2 is nonzero. To simplify the calculation, we assume that χ_2 in the decay is on shell, and as a result, we will focus on the light mediator case in this study, i.e., $\delta > m_V$.

- The elastically produced CRDM refers to CR-DM elastic scattering $p + \chi_1 \to p' + \chi_1$. In this situation, χ_2 is not present, and $\delta = 0$ as well.

We consider that the DM-proton cross section of the vector-vector interaction is rather a constant, independent of incoming proton energy. However, the CR spectrum rapidly decreases with CR energy. Except for the vector-vector interaction between fermionic DM and SM, there are more possible interaction types, and the velocity-dependent terms can also be important, which are beyond the popular (velocity-independent) spin-independent (SI) and spin-dependent (SD) form. Thus, we study several CRDM spectra based on different types of interactions to see the impact on the detected event rate. We investigate the exclusion power of the latest PandaX-4T data [5] in the region of the lower mass $m_{\chi_1} < 1\,\mathrm{GeV}$ and larger mass splitting $\delta \sim \mathcal{O}(\mathrm{GeV})$.

The remainder of this paper is organized as follows. First, we introduce several different types of DM-SM interactions in section 2 by considering both fermionic and scalar DM. In section 3, we describe the detection of elastic and inelastic DM-proton scattering for both vDM and CRDM. In section 4, we examine the interactions with the latest and most stringent exclusion from PandaX-4T. Finally, we conclude the study in section 5.

2 Effective inelastic DM interactions

To demonstrate our work, we consider minimum DM Lagrangians where a Z_2 even vector/axial vector mediator V[1] and a DM χ_1 with its excited state χ_2 are considered as the

---

[1]The leptophobic mediator V will mainly decay to mesons or quarks if kinematically allowed. For $m_V < m_\pi$, V can still decay to e^+e^-, $\nu\bar{\nu}$ via one loop process or $V - Z$ boson mixing. Note that the lifetime of V must be shorter than 1 second to avoid spoiling typical Big Bang nucleosynthesis history.
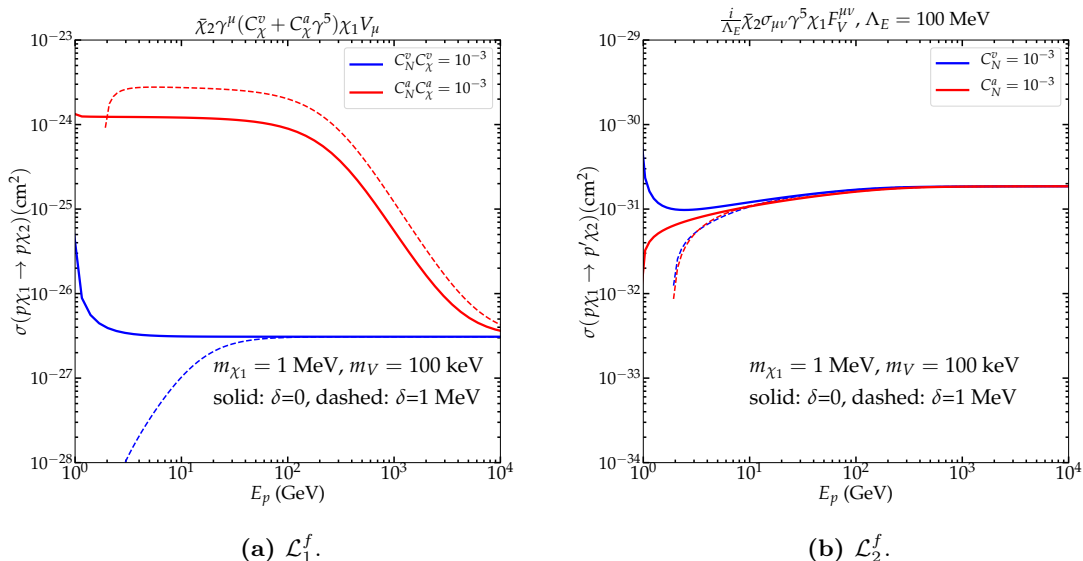
Figure 2. The integrated cross section of process $p\chi_1 \to p'\chi_2$ as a function of incoming proton energy E_p. We used red and blue lines to denote $C_N^v = 0$ and $C_N^a = 0$, respectively. Compared with the elastic scenario (solid lines), we also present $\delta = 1\,\text{MeV}$ as dashed lines. The AA interaction ($C_\chi^v = C_N^v = 0$) has a greater cross section than VV one ($C_\chi^a = C_N^a = 0$), while for $\mathcal{L}_2^f$, which is illustrated by ED, the resulting difference between the vector interaction and axial vector interaction of $\mathcal{L}_{VN}$ is small.

new implementation to the SM. We discuss both Majorana and real scalar DM fields in this study. The common nucleon-V interactions are:

$$\mathcal{L}_{VN} = \overline{N}\gamma^\mu \left(C_N^v + C_N^a\gamma^5 \right) N V_\mu. \tag{2.1}$$

The couplings C_N^v and C_N^a are for vector and axial vector interactions for nucleon. We require their sizes to be less than unity. Otherwise, the DM interaction with the nucleon would be so strong and be observed by detectors. The mediator V can be either a photon-like boson charged under the U(1) gauge or Z-like boson charged under SU(2) gauge. To maintain gauge invariance, ref. [30] indicates that if the boson V is SU(2) dark Z, the tree-level amplitude squared must be computed with a unitary gauge [31, 32], which will be considered in this study for both the vector and axial-vector interactions.

Next, we discuss interesting DM-V interactions $\mathcal{L}_{VD}$ and thus the completed Lagrangian to describe $p + \chi_1 \to p' + \chi_2$ process is $\mathcal{L}_{VN} + \mathcal{L}_{VD}$. Then, we focus on some characteristic types of Lagrangians for demonstration.

2.1 Fermionic DM interaction

For the fermionic DM scenario, two common types of effective interactions between DM and V are considered:

$$\mathcal{L}_1^f = \left[\overline{\chi_2}\gamma_\mu \left(C_\chi^v + C_\chi^a \gamma^5 \right) \chi_1 + h.c. \right] V^\mu, \tag{2.2}$$

$$\mathcal{L}_2^f = \frac{1}{\Lambda_{E(M)}} \bar{\chi}_2 \sigma_{\mu\nu} \Gamma_{E(M)} \chi_1 F_V^{\mu\nu}, \tag{2.3}$$

where $F_V^{\mu\nu} = \partial^\mu V^\nu - \partial^\nu V^\mu$, $\sigma_{\mu\nu} = \frac{i}{2}(\gamma^\mu\gamma^\nu - \gamma^\nu\gamma^\mu)$, electric dipole-like interaction $\Gamma_E = i\gamma_5$, and magnetic dipole-like interaction $\Gamma_M = 1$. The index f refers to the Majorana DM. The parameter $\Lambda_{E(M)}$ is the new physics scale and is a dimensional coupling that cannot be compared with C_χ^v or C_χ^a directly. Also, we only consider the product of $\chi\chi V$ and NNV couplings that appears in the scattering amplitude. Therefore, we can simply fix the coupling constants of the dark sector as constants $C_\chi^{v/a} = 1$ and $\Lambda_{E(M)} = 100$ MeV. We then compare the results based on different values of the NNV coupling, namely, C_N^v or C_N^a, and can easily rescale the result for other choices.

For simplicity, we focus on one type of interaction each time. In principle, there are four DM-SM interactions for $\mathcal{L}_1^f$: vector-vector (VV), vector-axial vector (VA), axial vector-vector (AV), and axial vector-axial vector (AA). Similarly, there are four possible DM-SM interactions for $\mathcal{L}_2^f$: vector-magnetic dipole (MD), axial vector-magnetic dipole, vector-electric dipole (ED), and axial vector-electric dipole. We choose the representative operators VV, AA, ED, and MD in this study because the VV and AA interaction predicts the minimal and maximum $p - \chi_1$ cross sections, respectively, and ED and MD are the most familiar DM models in the community.

The cross sections based on eq. (2.2) and eq. (2.3) are given in appendix B.2. For a comparison of axial vector and vector interaction in $\mathcal{L}_{VN}$, figure 2 shows an integrated cross section of the process $p\chi_1 \to p'\chi_2$ as a function of incoming proton energy E_p for each interaction of $\mathcal{L}_{VD}^f$. The solid lines represent the degenerate scenario ($m_{\chi_1} = m_{\chi_2}$), while the dashed lines are based on the inelastic cross section with $\delta = 1$ MeV. In figure 2a, the cross section of AA is higher than that of VV in the lower E_p region due to an additional contribution to the cross section of the AA, which dominates for small values of E_p. When the mediator mass is light, the enhancement is strong. Mass splitting can enhance axial vector interaction but suppress the vector interaction at the lower E_p region. However, in the large E_p region, all the interactions predict almost the same cross section. For dipole interactions of $\mathcal{L}_{VD}^f$, the resulting difference between the vector and axial vector in $\mathcal{L}_{VN}$ is less noticeable, as illustrated in figure 2b. Also, when mass splitting δ exists, there is a kinematic constraint on E_p for the inelastic scattering. More details are shown in appendix A. Therefore, the dashed lines do not start at $E_p = m_p$.

In figure 3, we show the integrated cross sections for $\mathcal{L}_1^f$ (left panel) and $\mathcal{L}_2^f$ (right panel) by comparison with three different mediator masses: $m_V = 10$ keV (blue lines), $m_V = 1$ MeV (black lines), and $m_V = 1$ GeV (red lines). As a demonstration, we only present the vector interaction (with $C_N^a = 0$) case while the cross section for the axial vector interaction will be larger, as shown in figure 2. Again, we use the solid line for the
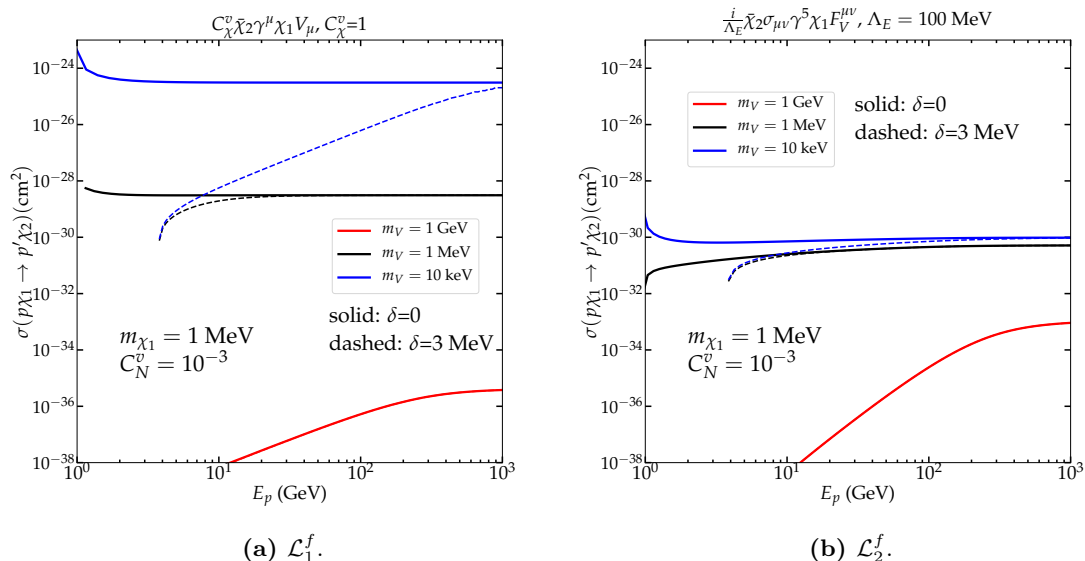
Figure 3. The integrated cross section for the process $p\chi_1 \to p'\chi_2$ with respect to the energy of incoming proton E_p for $\mathcal{L}_1^f$ (left panel) and $\mathcal{L}_2^f$ (right panel). Three mediator masses $10\,\mathrm{keV}$ (blue lines), $1\,\mathrm{MeV}$ (black lines), and $1\,\mathrm{GeV}$ (red lines) are shown. The difference between the red dashed line and red solid line are negligible. We only plot the SM vector interaction ($C_N^a = 0$) case as a demonstration.

degenerate scenario and the dashed line for the inelastic scattering. Generally, both the larger δ and larger m_V can suppress the cross section at the small E_p region, but the cross section will eventually be saturated in the high-energy region. When $\delta \gg m_V$, the cross section can even be suppressed up to the $E_p > 100$ GeV region (cf. blue dashed line in panel (a)). Comparing two different fermionic DM interactions, the suppression due to δ is more severe in the $\mathcal{L}_1^f$ than $\mathcal{L}_2^f$ for the light m_V case.

2.2 Scalar DM interaction

Regarding the interactions between the spin-zero inelastic scalar DM and the vector mediator, we also consider two benchmarks:

$$\mathcal{L}_1^s = g_\chi(\chi_1 \partial^\mu \chi_2 - \chi_2 \partial^\mu \chi_1)V_\mu, \tag{2.4}$$

$$\mathcal{L}_2^s = \frac{1}{\Lambda_s^2}(\partial_\mu \chi_2 \partial_\nu \chi_1)F_V^{\mu\nu}. \tag{2.5}$$

As a comparison, the dipole-like interaction eq. (2.5) is considered. The index s denotes scalar DM. As mentioned above, only the product of the DM and SM couplings appears in the cross section. We therefore only alter the SM coupling constant C_N^v and C_N^a in eq. (2.2) and fix the coupling constants of the dark sector as $g_\chi = 1$ and $\Lambda_s = 100$ MeV.

In figure 4, we compare the integrated cross section for $\mathcal{L}_1^s$ (left panel) and $\mathcal{L}_2^s$ (right panel). The color scheme is the same as figure 2. Fixing the vector interaction of SM part, $\mathcal{L}_1^s$ leads to an almost identical cross section as the fermionic case $\mathcal{L}_1^f$ by comparing the
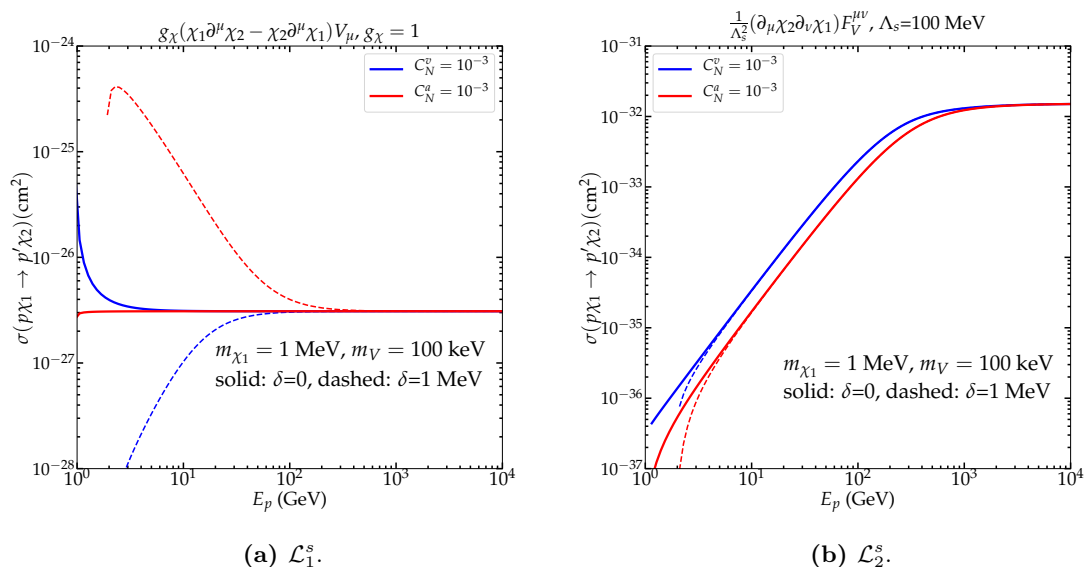
Figure 4. The integrated cross section between scalar DM and an incoming proton as a function of its energy E_p. A nonzero δ contributes to an enhancement for Lagrangian $\mathcal{L}_1^s$ with SM axial vector interaction. For $\mathcal{L}_2^s$, the resulting difference between the SM vector and axial vector interaction is tiny.

blue lines in figure 2a and 4a. This result is due to the similarity of their amplitude squared structure. Conversely, for fixing the SM axial vector interaction, the $\delta = 0$ case for $\mathcal{L}_1^s$ (red solid line) differs from the one for $\mathcal{L}_1^f$, where the former is flat, but an enhancement appears in the latter. This result is due to the nontrivial behavior of amplitude squared of axial vector interaction with the unitary gauge. When fixing the SM axial vector, we observe that both the DM interactions $\mathcal{L}_1^f$ and $\mathcal{L}_1^s$ lead to cross sections with the same order using the same coupling strength if E_p increases sufficiently. Also, when $\delta = 0$, the enhancement of $\mathcal{L}_1^s$ vanishes but remains for $\mathcal{L}_1^f$. This enhancement is actually only important for a light mediator mass. For dipole form interaction $\mathcal{L}_2^s$, as shown in figure 4b, the cross section is generally suppressed at the lower E_p region. In addition, the inelastic scattering cross section does not differ markedly from that of elastic scattering.

In figure 5, we plot the inelastic scalar DM scenario with the same scheme as in figure 3. With a similar amplitude squared structure, figure 3a and 5a are almost identical, even if their spins are different. For $\mathcal{L}_2^s$ as shown in figure 5b, we can see that the cross section is not sensitive to δ at all. However, the cross section is sensitive to m_V only for large m_V (red lines), where its value is markedly suppressed.

3 Detection of vDM and CRDM

In this section, we first review the formulas of traditional inelastic DM scattering with the target nuclei. vDM is present around the Earth with a local density $\rho_0 = 0.3\,\mathrm{GeV \cdot cm^{-3}}$, and its velocity distribution can be simply described by a soft truncated Maxwell-Boltzmann
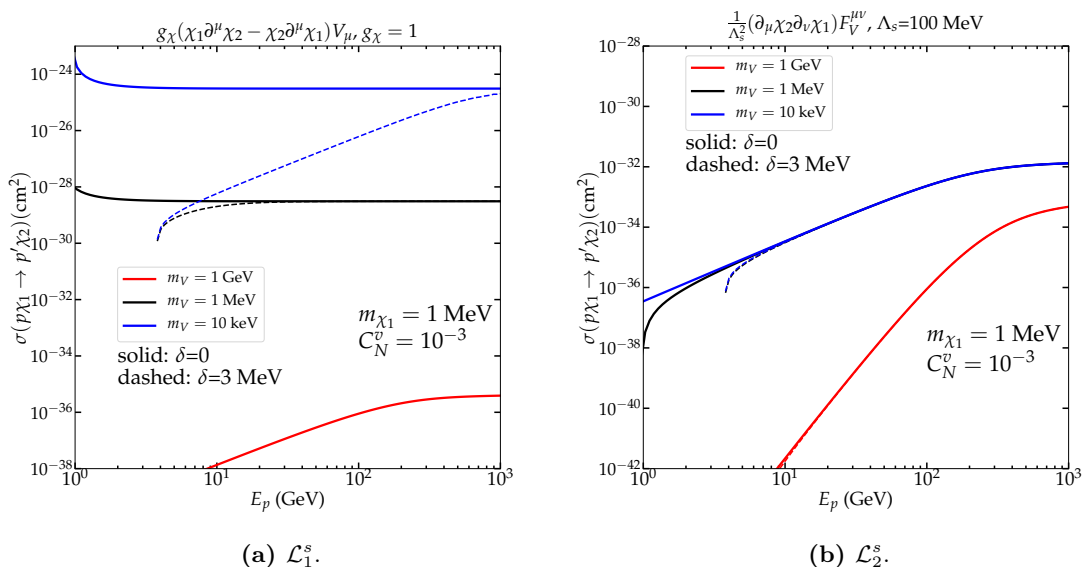
Figure 5. Same as in figure 3 but for scalar DM scenario. The left and right panels are for the interactions $\mathcal{L}_1^s$ and $\mathcal{L}_2^s$, respectively.

form. In the second part of this section, the inelastic CRDM fluxes $d\phi_\chi/dT_\chi$ during the CR-DM collisions, which can be altered with respect to different values of m_{χ_1} and δ, are investigated. Finally, we estimate the detected inelastic DM event rate $\mathcal{R}$ of the CRDM scattering with the target nuclei.

3.1 Traditional detection of the virialized DM

We first consider the case of vDM. The Earth sweeps the local DM halo, where DMs are virialized, and their velocity v can be well described by a Maxwell-Boltzmann distribution $f(v)$. Following the convention of ref. [33], the differential event rate of scattering between DM and the target nucleus *per unit detector mass* with respect to the recoil energy Q can be written as:

$$\frac{\mathrm{d}\mathcal{R}}{\mathrm{d}Q} = \sum_{\mathcal{T}} \xi_{\mathcal{T}} \frac{\rho_0}{m_{\chi_1} m_{\mathcal{T}}} \int_{v > v_{\min}(Q)} v f(v) \frac{\mathrm{d}\sigma_{\chi\mathcal{T}}}{\mathrm{d}Q} \, d^3v, \tag{3.1}$$

where the parameter $\xi_{\mathcal{T}}$ is defined as:

$$\xi_{\mathcal{T}} = \frac{\eta_{\mathcal{T}} m_{\mathcal{T}}}{\sum_{\mathcal{T}} \eta_{\mathcal{T}} m_{\mathcal{T}}}. \tag{3.2}$$

The isotope fraction $\eta_{\mathcal{T}}$ can also be found online.[2] The target mass $m_{\mathcal{T}}$ depends on the material used in the detectors. The momentum transfer $\mathbf{q}$ differs from the recoil energy Q but are related by $\mathbf{q}^2 = 2m_{\mathcal{T}}Q$. For a mass splitting δ between χ_1 and χ_2, the kinetic phase space in the inelastic process will be restricted by a minimum velocity, which is determined

---

[2]https://www.webelements.com/xenon/.

by taking the limits of small δ and v:

$$v_{\min}(Q) = \frac{1}{\sqrt{2m_{\mathcal{T}}Q}}\left(\frac{m_{\mathcal{T}}Q}{\mu_{\chi N}} + \delta\right), \tag{3.3}$$

where $\mu_{\chi N}$ is the dark matter-nucleon reduced mass. Taking the nonrelativistic limit $T_{\chi_1} = m_{\chi_1}v^2/2$ and one-dimensional velocity distribution, eq. (3.1) in terms of the DM fluxes $d\phi_\chi/dT_\chi = \rho_0 f(v)/m_{\chi_1}^2$ returns the general form:

$$\frac{\mathrm{d}\mathcal{R}}{\mathrm{d}Q} = \sum_{\mathcal{T}} \frac{\xi_{\mathcal{T}}}{m_{\mathcal{T}}} \int_{T_\chi[v_{\min}(Q)]} \frac{d\phi_\chi}{dT_\chi}\frac{\mathrm{d}\sigma_{\chi\mathcal{T}}}{\mathrm{d}Q}\, dT_\chi. \tag{3.4}$$

In the limit $v \to 0$, the cross section $\mathrm{d}\sigma_{\chi\mathcal{T}}/\mathrm{d}Q$ includes spin-independent (SI) and spin-dependent (SD) components. The SI component can also be coherently enhanced by target atom number square $\mathcal{A}^2$, particularly:

$$\frac{\mathrm{d}\sigma_{\chi\mathcal{T}}^{\mathrm{SI}}}{\mathrm{d}Q} = \frac{\mathrm{d}\sigma_{\chi p}^{\mathrm{SI}}}{\mathrm{d}Q} \times \frac{\mu_{\mathcal{A}}^2}{\mu_p^2} \times \left[\mathcal{Z} + \frac{f_n}{f_p}\left(\mathcal{A} - \mathcal{Z}\right)\right]^2 \times F^2(Q, \mathcal{A}, \mathcal{Z}), \tag{3.5}$$

where μ_p^2 and $\mu_{\mathcal{A}}^2$ are the DM-proton and DM-atom reduced masses, respectively, and for isospin conservation, $f_p = f_n$. When using a velocity- and spin-independent cross section in this study, we only take the Helm type form factor for $F^2(Q, \mathcal{A}, \mathcal{Z})$ as ref. [34].

Finally, theoretically predicted events can be compared with experimental measurements by including the efficiency of the underground detector $\epsilon(Q)$ to account for the experimental analysis. Thus, the total event rate is:

$$\mathcal{R} = \int_0^\infty \epsilon(Q)\frac{\mathrm{d}\mathcal{R}}{\mathrm{d}Q}dQ. \tag{3.6}$$

3.2 Inelastic production of CRDM

The vDMs near the Earth are non-relativistic, and their mean and escape velocities are approximately 240 km s^{-1} and 540 km s^{-1} [4, 35, 36]. However, DM may be accelerated by high-energy CR protons toward the Earth with a relativistic velocity. If the masses of χ_1 and χ_2 differ by a small mass splitting δ, such a high energy transfer from CR can excite χ_1 to χ_2. The inelastic DM collision with the CR proton can be described as:

$$p + \chi_1 \to p' + \chi_2 \to p' + \chi_1 + V, \tag{3.7}$$

where p is a cosmic proton and V is a Z_2 even boson mediated between SM and dark sectors. To ensure that V is produced on the shell, we require $\delta > m_V$ throughout this study. Compared with the nonrelativistic vDM originating from our neighborhood, the CRDM produced by $p\chi_1$ scattering may occur everywhere in our galaxy. Similar to refs. [21, 22], the DM flux caused by $p\chi_1$ scattering is:

$$\frac{d\phi_{\chi_1}^{\mathrm{MW}}}{dT_{\chi_1}} = \int d\Omega \int_{\mathrm{l.o.s.}} d\ell \int dE_p \frac{\rho_\chi(r)}{m_{\chi_1}}\frac{d\phi_p}{dE_p}\frac{d\sigma_{p\chi_1 \to p'\chi_1 V}}{dT_{\chi_1}}, \tag{3.8}$$

where we take the Navarro-Frenk-White halo profile for illustration and the DM halo density is defined as ρ_χ. The integration is performed along the line of sight (l.o.s.). The distribution $d\sigma_{p\chi_1 \to p'\chi_1 V}/dT_{\chi_1}$ describes the differential cross section of the collision process given in eq. (3.7) with respect to kinetic energy of the final state χ_1. The differential flux of CR protons $d\phi_p/dE_p$ is in units of GeV^{-1} cm^{-2} s^{-1} sr^{-1}.

In ref. [28], they compared two different CR proton spatial distributions: one with a uniform and isotropic distribution in a cylinder, and the other with the actual simulation resulting from GALPROP [37]. However, the differences in the accelerated DM fluxes between these two results are small. Therefore, we can follow refs. [22, 24, 26, 28] to assume that the CR proton distribution is uniform and isotropic in a cylinder with radius $R = 10$ kpc and half-height $h = 1$ kpc. The spectra for protons and helium are taken from ref. [38] for $E_p \lesssim 10^6$ GeV (below the first knee). We can also use the CR fluxes approximately described by a broken power law $d\phi_p/dE_p \propto E_p^{-\gamma}$, where $\gamma \approx 3$ for $10^6 \lesssim E_p \lesssim 2 \times 10^8$ GeV (below the second knee), and $\gamma \approx 3.3$ for $2 \times 10^8 \lesssim E_p \lesssim 3 \times 10^9$ GeV (below the ankle). Also, we can neglect the $E_p > 3 \times 10^9$ GeV flux due to Greisen-Zatsepin-Kuzmin cutoff [39]. Because we only take the spatial independent $d\phi_p/dE_p$, we can simplify the standard DM fluxes eq. (3.8) by integrating the DM halo density:

$$\frac{d\phi_{\chi_1}^{\mathrm{MW}}}{dT_{\chi_1}} = \frac{\rho_0}{m_{\chi_1}} \times D_{\mathrm{eff}} \times \sum_{i=p,\mathrm{He}} \int dE_i \frac{d\phi_i}{dE_i} G_i^2(2m_{\chi_1}T_{\chi_1}) \frac{d\sigma_{p\chi_1 \to p'\chi_1 V}}{dT_{\chi_1}}, \qquad (3.9)$$

where D_{eff} is the effective length:

$$D_{\mathrm{eff}} = \int d\Omega \int_{\mathrm{l.o.s.}} \frac{\rho[r(\ell,\Omega)]}{\rho_0} d\ell. \qquad (3.10)$$

The $G_i^2(Q^2)$ here is simply taken in its dipole form:

$$G_i^2(Q^2) = \left[1 + \frac{Q^2}{\Lambda_i^2} \right]^{-4}, \qquad (3.11)$$

where $\Lambda_p = 770\,\mathrm{MeV}$ and $\Lambda_{\mathrm{He}} = 410\,\mathrm{MeV}$.

Because the process used in eq. (3.7) is a $2 \to 3$ process with on-shell produced χ_2, we can simply used a narrow width approximation to break down the Feynman diagram to $p\chi_1 \to p'\chi_2$ and $\chi_2 \to \chi_1 V$. Therefore, the distribution of the cross section can be written as:

$$\frac{d\sigma_{p\chi_1 \to p'\chi_1 V}}{dT_{\chi_1}} = \int \frac{d\sigma_{p\chi_1 \to p'\chi_2}}{dT_{\chi_2}} \frac{dT_{\chi_2}}{dT_{\chi_1}} \frac{dB_{\chi_2 \to \chi_1 V}}{d\cos\theta'} d\cos\theta', \qquad (3.12)$$

where θ' is the angle between the χ_2 direction in the lab frame of the $p\chi_1$ and χ_1 directions for $\chi_2 \to \chi_1 V$ decay in the χ_2 rest frame. The differential cross section $d\sigma_{p\chi_1 \to p'\chi_2}/dT_{\chi_2}$ and expression of $dB_{\chi_2 \to \chi_1 V}$ are shown in appendix B.

Next, we need a Jacobian dT_{χ_2}/dT_{χ_1}. Considering the process of $\chi_2 \to \chi_1 + V$, we can express the final T_{χ_1} by initial E_{χ_2} in the lab frame:

$$T_{\chi_1} = \frac{E_{\chi_1}^* E_{\chi_2} + |\mathbf{p}_{\chi_1}^*| \sqrt{E_{\chi_2}^2 - m_{\chi_2}^2} \cos\theta'}{m_{\chi_2}} - m_{\chi_1}, \qquad (3.13)$$
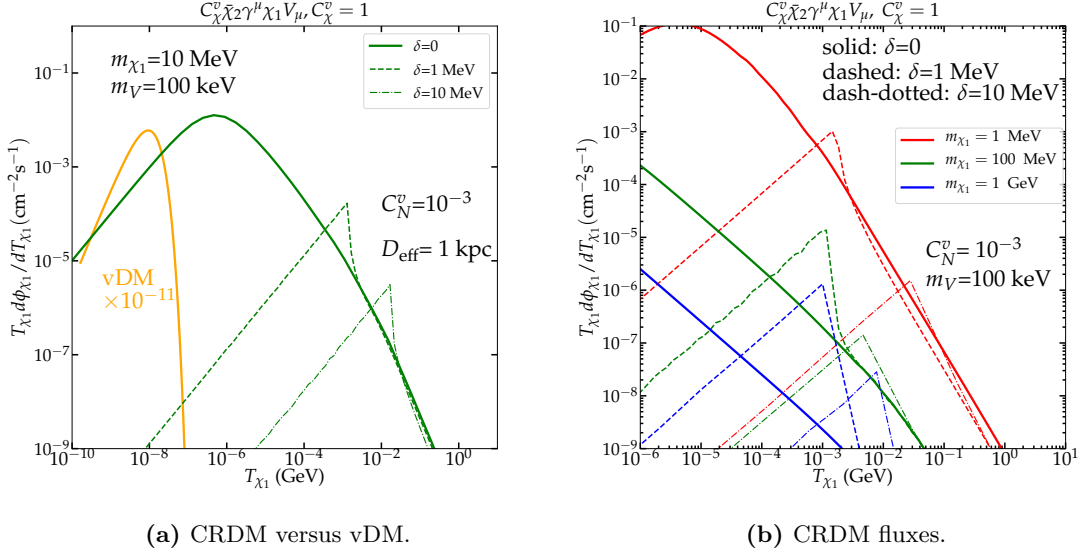
(a) CRDM versus vDM.

(b) CRDM fluxes.

Figure 6. (a) Comparison of vDM and CRDM fluxes. Both vDM and CRDM fluxes are obtained by using $\bar{\chi}_2 \gamma^\mu \chi_1 V_\mu$ interaction with $m_{\chi_1} = 10 \,\text{MeV}$, $m_V = 100 \,\text{keV}$, and $C_N^a = 10^{-3}$. The value of D_{eff} for CRDM is fixed to 1 kpc as a default value. (b) Spectra of CRDM with the VV interaction. Three benchmarks of DM mass 1 MeV (red lines), 100 MeV (green lines), and 1 GeV (red lines) are presented. We also plot three different mass splittings, $\delta = 0$ (solid lines), $\delta = 1 \,\text{MeV}$ (dashed lines), and $\delta = 10 \,\text{MeV}$ (dash-dotted lines).

where $E_{\chi_1}^* = (m_{\chi_1}^2 + m_{\chi_2}^2 - m_V^2)/(2m_{\chi_2})$ and $|\mathbf{p}_{\chi_1}^*| = \sqrt{E_{\chi_1}^{*2} - m_{\chi_1}^2}$ are the energy and momentum of χ_1 in the χ_2 rest frame. By inverting eq. (3.13), one can obtain the expression of T_{χ_2} as:

$$T_{\chi_2}(T_{\chi_1}, \cos\theta') = \frac{m_{\chi_2} E_{\chi_1}^* (m_{\chi_1} + T_{\chi_1})}{(E_{\chi_1}^*)^2 - (|\mathbf{p}_{\chi_1}^*|\cos\theta')^2} - m_{\chi_2}$$
$$- \frac{m_{\chi_2}|\mathbf{p}_{\chi_1}^*|\cos\theta' \sqrt{(m_{\chi_1} + T_{\chi_1})^2 - (E_{\chi_1}^*)^2 + (|\mathbf{p}_{\chi_1}^*|\cos\theta')^2}}{(E_{\chi_1}^*)^2 - (|\mathbf{p}_{\chi_1}^*|\cos\theta')^2}. \quad (3.14)$$

We can differentiate the above equation to obtain dT_{χ_2}/dT_{χ_1}:

$$\frac{dT_{\chi_2}}{dT_{\chi_1}} = \frac{m_{\chi_2}}{(E_{\chi_1}^*)^2 - (|\mathbf{p}_{\chi_1}^*|\cos\theta')^2} \times \left[E_{\chi_1}^* - \frac{|\mathbf{p}_{\chi_1}^*|\cos\theta'(m_{\chi_1} + T_{\chi_1})}{\sqrt{(m_{\chi_1} + T_{\chi_1})^2 - (E_{\chi_1}^*)^2 + (|\mathbf{p}_{\chi_1}^*|\cos\theta')^2}} \right]. \quad (3.15)$$

For illustration, we calculate the fluxes of several characteristic interactions by applying eq. (3.12). Because the difference of SM axial vector and vector interaction has already been discussed (figure 2 and figure 4), we only display the situation of vector interaction and focus on the effects of kinematic variables. Additionally, we do not show the flux generated by $\mathcal{L}_1^s$, from which the resulting cross section is similar to the VV cross section.

In figure 6, we compare the vDM flux (orange solid line) with CRDM fluxes (green lines) using $m_{\chi_1} = 10 \,\text{MeV}$, $m_V = 100 \,\text{keV}$, and $C_N^v = 10^{-3}$ (left). We use VV interaction

– 11 –

for CRDM as a demonstration, but the shapes for other interactions do not differ much except for their scales. For CRDM, we take $D_{\text{eff}} = 1$ kpc as a default value. The green solid line represents elastic scattering with $m_{\chi_1} = m_{\chi_2}$, but the dashed and dashed-dotted lines describe the mass splitting $\delta = 1\,\text{MeV}$ and $\delta = 10\,\text{MeV}$, respectively. We note that a larger mass splitting makes a stronger suppression for the lower T_{χ_1}. We can clearly see that the fluxes of vDM in the figure 6a peaks at approximately $10^{-8}\,\text{GeV}$, where DM has a nonrelativistic velocity around $10^{-3}c$. As an expected feature from CRDM, its T_{χ_1} can be comparable with m_{χ_1}, where DM is relativistic particle. In fact, light vDM, such as $m_{\chi_1} = 10$ MeV, is not detectable for the present underground experiments due to its low kinetic energy. However, both elastic and inelastic CRDM obtain enough energy to be observed. Also, we can see that the magnitude of fluxes of vDM can be approximately 11 orders higher than CRDM, which occurs because the integrated cross section of CR collision with DM is small ($\sim 10^{-27}\,\text{cm}^2$), even if the CRDM fluxes are accumulated over the line of sight, particularly D_{eff}. The current powerful PandaX-4T and XENON1T detectors are thus capable of testing such events.

We also show the CRDM fluxes with three different DM masses and splittings in figure 6b. We use three benchmarks of DM mass $1\,\text{MeV}$ (red lines), $100\,\text{MeV}$ (green lines), and $1\,\text{GeV}$ (blue lines). For the three mass splittings, the solid, dashed, and dash-dotted lines correspond to the mass-degenerated case, $\delta = 1\,\text{MeV}$, and $\delta = 10\,\text{MeV}$, respectively. We can see that all the mass-degenerated cases have smooth curves, but those non-degenerated curves show sharp peaks at T_{sp}. The spectrum follows the CR spectrum at the $T_\chi > T_{\text{sp}}$ region but also has a markedly different shape from the CR shape in the $T_\chi < T_{\text{sp}}$ region. As shown in eq. (3.9), the CRDM energy spectrum is the product of the distribution $d\sigma_{p\chi_1}/dT_{\chi_1}$ and CR energy spectrum. We also show in figures 2, 3, 4, and 5 that the cross section is flat at high energy, but the δ contribution dominates $d\sigma_{p\chi_1}/dT_{\chi_1}$ in the lower energy region. Thus, in the small energy region $T_\chi < T_{\text{sp}}$, the spectrum is strongly affected by $d\sigma_{p\chi_1 \to p'\chi_1 V}/dT_{\chi_1}$.

For the CRDM with $\delta = 0$, its energy is only provided by $p\chi_1$ elastic collision. Moreover, a final state χ_1 can be boosted by δ owing to the χ_2 decay after the inelastic $p\chi_1 \to p'\chi_2$ process, as also mentioned in ref. [29]. Therefore, the CRDM flux with a larger δ can depart from the mass-degenerate scenario toward higher energy. *Thus, δ can cause a sharp peak T_{sp} in the spectrum toward higher energy but with a decline of total flux.*

For dipole-like operators, we show the CRDM fluxes for fermionic DM cases (two upper panels) and scalar DM cases (two lower panels) In figure 7. The left panels show the light mediator scenarios ($m_V = 100\,\text{keV}$), while the right panels show the heavy mediator scenario ($m_V = 10\,\text{MeV}$). We use the same color scheme as figure 6b, and the important features such as the shifts of the shark peaks are also mentioned previously. Comparing with the VV interaction in figure 6b, the spectra of the elastic scattering of all dipole-like interactions are softer. Therefore, the fluxes of the sharp peaks created by χ_2 decay ($\delta \neq 0$) are generally lower than $\delta = 0$ case in the dipole-like interactions. Finally, the flux of the scalar dipole-like DM interaction is lower than that of the fermionic interaction when using the same values of couplings. Note that $C_N^v = 10^{-1}$ for the former and $C_N^v = 10^{-2}$ for the latter.
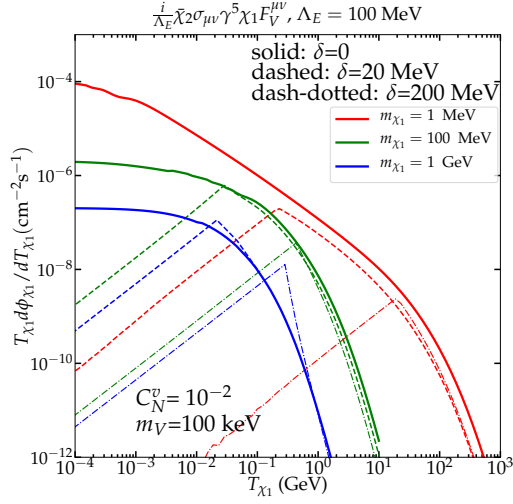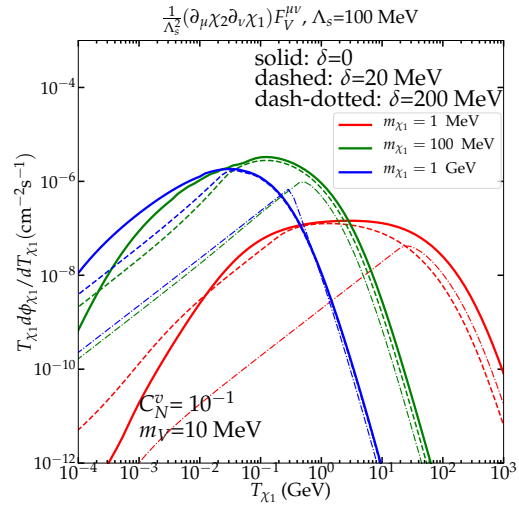
(a) Fermionic DM with $m_V = 100\,\mathrm{keV}$.
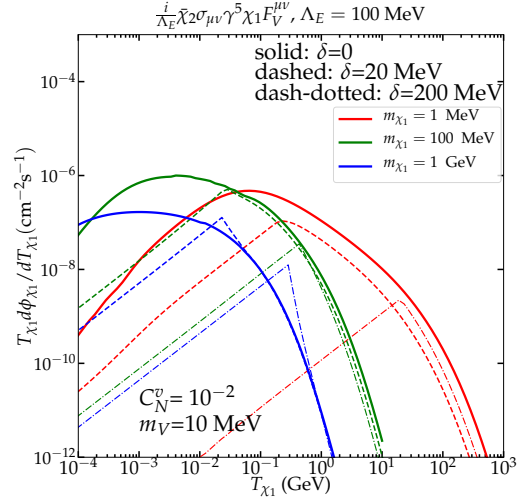
(b) Fermionic DM with $m_V = 10\,\mathrm{MeV}$.
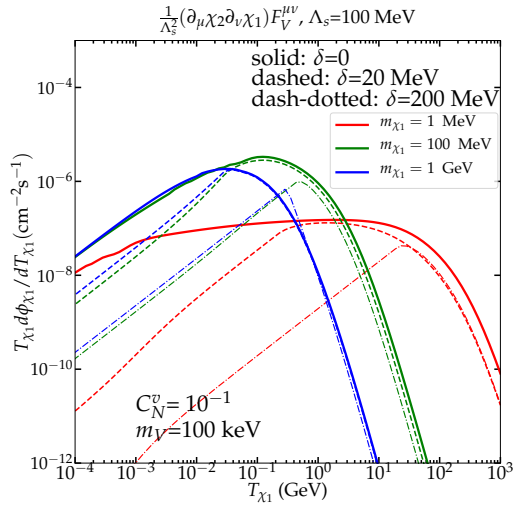
(c) Scalar DM with $m_V = 100\,\mathrm{keV}$.

(d) Scalar DM with $m_V = 10\,\mathrm{MeV}$.

Figure 7. Energy spectra of CRDM for $\mathcal{L}_2^f$ (upper panels) and $\mathcal{L}_2^s$ (lower panels). The mediator masses applied here are $m_V = 100\,\mathrm{keV}$ (left figures) and $m_V = 10\,\mathrm{MeV}$ (right figures). The color scheme is the same as figure 6b.

(a) VV and AA interactions.
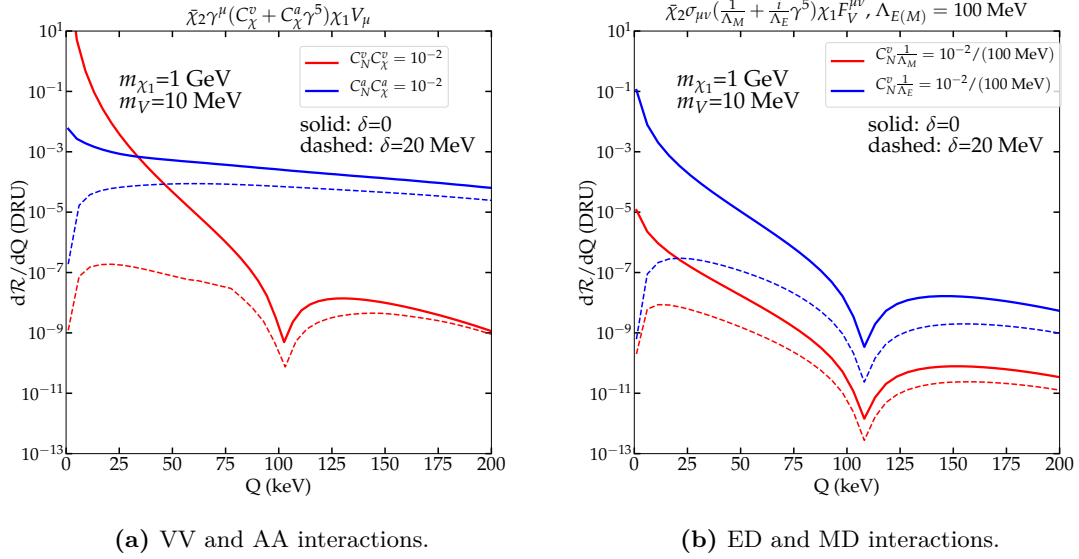
(b) ED and MD interactions.

Figure 8. Detection rate $d\mathcal{R}/dQ$ (DRU or $\text{keV}^{-1}\text{kg}^{-1}\text{day}^{-1}$) of fermionic CRDM χ−xenon scattering for $\mathcal{L}_1^f$ (left) and $\mathcal{L}_2^f$ (right). The mass degenerated cases $\delta = 0$ are represented as solid lines, while the dashed lines are for $\delta = 20\,\text{MeV}$.

3.3 CRDM detection rate

Following the conventions of refs. [21, 40], we can write down the differential recoil rate per target nucleus of relativistic DM in underground detectors:

$$\frac{d\mathcal{R}}{dQ} = \sum_{\mathcal{T}} \frac{\xi_{\mathcal{T}}}{m_{\mathcal{T}}} \int_{T_{\min}}^{\infty} dT_{\chi_1} \frac{d\sigma_{\chi_1 \mathcal{T}}}{dQ} \frac{d\Phi_{\chi_1}^{\text{MW}}}{dT_{\chi_1}}, \tag{3.16}$$

where $T_{\min}$ is the minimum kinetic energy of incoming DM, and only $\mathcal{T}$ =xenon is used in this study. For those DM that strongly interact with nuclei, $T_{\min}$ can be varied with respect to the DM length of propagation in the Earth and the DM-nuclei cross section in the attenuation process. When the attenuation effect is negligible, the $T_{\min}$ only depends on the kinematics, as shown in appendix. A.

As shown in section 3.1, the final $d\sigma_{\chi N}/dQ$ has to be the product of the χp cross section and the form factor as performing in eq. (3.5). However, the form factor for the SI or SD cross section is derived by velocity-independent technology. As shown in refs. [41–45], a velocity-dependent collision (e.g., dipole interaction) sometimes contains more than these two contributions. Therefore, we use the effective operator method developed by refs. [41–45] to extract the complete form factor for our inelastic interactions. In these studies, the leading order of the velocity contribution was used. Considering that the form factor relates $\sigma_{\chi p}$ to $\sigma_{\chi \mathcal{T}}$, the inelastic cross section of DM-target scattering is:

$$\frac{d\sigma_{\chi \mathcal{T}}}{dQ}(m_{\chi_1}, \delta, m_V, Q) = \frac{d\sigma_{\chi \mathcal{T}}}{dQ}\bigg|_{\text{EFT}} \times \frac{\mathcal{M}_{\chi p}^2(m_{\chi_1}, \delta, m_V, Q)}{\mathcal{M}_{\chi p, \text{EFT}}^2} \tag{3.17}$$

– 14 –

where the effective operator cross section $\frac{d\sigma_{\chi\mathcal{T}}}{dQ}|_{\text{EFT}}$ is obtained with the publicly available numerical code `LikeDM-DD` [33]. $\mathcal{M}^2_{\chi p}(m_{\chi_1}, \delta, m_V)$ are calculated in appendix B, but $\mathcal{M}^2_{\chi p,\text{EFT}}$ is used with $\delta = 0$ and the limit $m_V \gg Q$.

Because the form factors are independent of m_V and δ, eq. (3.17) is valid. The VV, AA, MD, and ED interactions in the effective theory limit correspond to the effective operators $\mathcal{Q}^{(6)}_1$, $\mathcal{Q}^{(6)}_4$, $\mathcal{Q}^{(5)}_1$, and $\mathcal{Q}^{(5)}_2$ in ref. [33], respectively. Only the fermionic DM cases are presented here because the result for scalar interaction $\mathcal{L}^s_1$ is similar to that of the VV interaction, and $\mathcal{L}^s_2$ is markedly suppressed by Λ^2_s.

We now show the predicted event rate with fermionic VV (red lines in figure 8a), AA (blue lines in figure 8a), MD (red lines in figure 8b) and ED (blue lines in figure 8b) interactions. We can clearly see a dip in the curves of VV, ED, and MD whose form factor contains a significant contribution from the SI component. The AA interaction may contain the SD component without $\mathcal{A}^2$ enhancement, but the CRDM fluxes of AA interaction are generally higher than those of VV so that the AA event rate is not much lower than VV at the lower recoil range in the elastic case. When $Q > 40\,\text{keV}$, the spectrum of AA can be even higher than that of VV by using the same parameters. Generally, in the elastic case, the AA interaction predicts the highest event rate at high Q, but VV predicts the highest at the low Q. Due to the new physics scale $\Lambda_{E(M)}$ suppression, the dipole-like interactions ED and MD generally lead to a lower rate. Also, splitting δ can reduce the detected rate, and AA predicts the highest rate for $\delta = 20\,\text{MeV}$. Thus, unlike elastic scattering scenario, the target xenon is more sensitive to detect the AA inelastic scattering cross section than the VV interaction, even if the AA interaction may not depend on the SI form factor enhanced by coherence.

Comments about the attenuation of the DM flux during propagation. In this study, we ignore the attenuation effect from the Earth but focus on the exclusion limits, as in ref. [29]. In principle, a simple version of transport equations should at least include the propagation of χ_1 and χ_2. For the elastic CRDM scenario, attenuation is important for $\sigma_{\chi p} > \mathcal{O}(10^{-28})\,\text{cm}^2$ [21–24, 26]. However, it is difficult to know for inelastic scattering without a simulation. Considering the same cross section for both $\delta = 0$ and $\delta > 0$ scenarios, the inelastic DM can lose its energy much more efficiently than elastic DM because of $\chi_1 \to \chi_2$ excitation and χ_2 decay. Conversely, if using the same coupling for these two scenarios, the cross section for the $\delta > 0$ case may be lower than that for $\delta = 0$, such as for the VV case.

Quantitatively, a numerical code that simulates the energy distribution of χ_1 and χ_2 after their propagation should be developed but is beyond the scope of this study. Our research team plans to return to this issue in the future with a novelly designed numerical code.

4 Current constraints from PandaX-4T

The current, most stringent limitation of the DM-proton scattering cross section is from PandaX-4T [5]. The DM-proton elastic scattering cross section $\sigma_{\chi p}$ above 3.3×10^{-47} cm^2

at DM mass $\sim 30\,\mathrm{GeV}$ is excluded in 90%C.L. with 3.7 tons of liquid xenon target and an exposure of 0.63 tonne×year. However, such a limit is only applicable to elastic vDM. To apply to inelastic and relativistic DM scenarios, we must restore the limit of event rate $\mathcal{R}$ rather than that of $\sigma_{\chi p}$.

Thus, we can recast the PandaX-4T 90% C.L. of event rate in the following. First, we insert the published $\sigma_{\chi p}$ values of PandaX-4T 90% C.L. into eq. (3.1) and eq. (3.6), Then, the event rates for a fixed DM mass can be determined. Actually, the published PandaX-4T exclusion plot is based on the recoil energy spectra, which is related to the incoming DM kinetic energy. In this study, we use the efficiency curve from ref. [46], and the window of the maximum efficiency is located for the detected recoil energies between $20\,\mathrm{keV}$ and $100\,\mathrm{keV}$. The total event rate with an incoming DM momentum larger than threshold energy $30\,\mathrm{MeV}$ ($m_{\chi_1} = 30\,\mathrm{GeV}$ with DM velocity $10^{-3}c$) is found to be nearly constant at $\mathcal{R} \sim 4/0.63/\mathrm{tonne/year}$. However, $\mathcal{R}$ varies rapidly when the incoming DM momentum is smaller than $30\,\mathrm{MeV}$. Thus, we use $\mathcal{R} \sim 4/0.63/\mathrm{tonne/year}$ projected onto the (δ, C_N) and (m_{χ_1}, δ) planes to show the detection capability of PandaX-4T.

Results are shown in figure 9. Generally, there are four unknown variables that we are interested in: m_{χ_1}, δ, m_V and the coupling strength $C_N = C_N^{a/v}$. Again, we take $D_{\mathrm{eff}} = 1$ kpc, $C_\chi^v = C_\chi^a = 1$, and $\Lambda_{E(M)} = 100\,\mathrm{MeV}$ for dipole-like interaction here. As a reference, the $p\chi_1 \to p'\chi_2$ cross section with $C_N^{v/a} \approx 10^{-3}$ for VV and AA, respectively, and $C_N^v \approx 10^{-2}$ for both MD and ED at a high E_p are approximately equal to $\mathcal{O}(10^{-28})\,\mathrm{cm}^2$.

In figure 9a and 9b, by fixing m_{χ_1} and m_V, we obtain the limits of C_N for each δ and the VV (blue solid line), AA (red dash-dotted line), ED (green dashed line), and MD (purple dotted line) interactions. An interesting feature is that the exclusion lines of C_N remain relatively flat when the mass splitting is less than a given value near $\delta \lesssim 10\,\mathrm{MeV}$. *Thus, if δ is comparable to m_V, the total event rate is no longer sensitive to the changes of δ.* However, δ larger than $10\,\mathrm{MeV}$ can weaken the limit. As mentioned in the former sections, a larger δ can reduce the inelastic CRDM event rate. Compared with the inelastic vDM scenario as the result from [20], the inelastic CRDM helps us to probe a larger δ region. When increasing m_{χ_1}, the limits for the interactions with a γ^5 (AA and ED) at the region $\delta < 10^{-2}\,\mathrm{GeV}$ are markedly improved, but the limit for the MD interaction can be even weaker. In the large δ region, PandaX-4T rapidly loses exclusion power if considering a large m_{χ_1}. Because the order of coupling strength can also represent the related size of the DM-proton cross section, the PandaX-4T result projected on the AA interaction can give the most stringent limit on C_N while the higher dimensional operators, especially MD, have weaker limits.

Figure 9c and 9d show the exclusion limits from PandaX-4T projected to the (m_{χ_1}, δ) plane. Due to the on-shell condition $\delta > m_V$, the pink region is not accessible. Based on the information of figure 9a and 9b, we arbitrarily fix their couplings to optimize their detection as closer as the PandaX-4T limit at $\delta \to 0$. In figure 9c, we find that only the exclusion region of the AA interaction is between two red dash-dotted lines, while the exclusion regions are below the corresponding lines for other interactions. These results occur because mass splitting (see figure 2a) plays a role of enhancement in AA interaction. The bottom left corner with $\delta < 5 \times 10^{-2}\,\mathrm{GeV}$ and $m_{\chi_1} < 2 \times 10^{-3}\,\mathrm{GeV}$ becomes an allowed
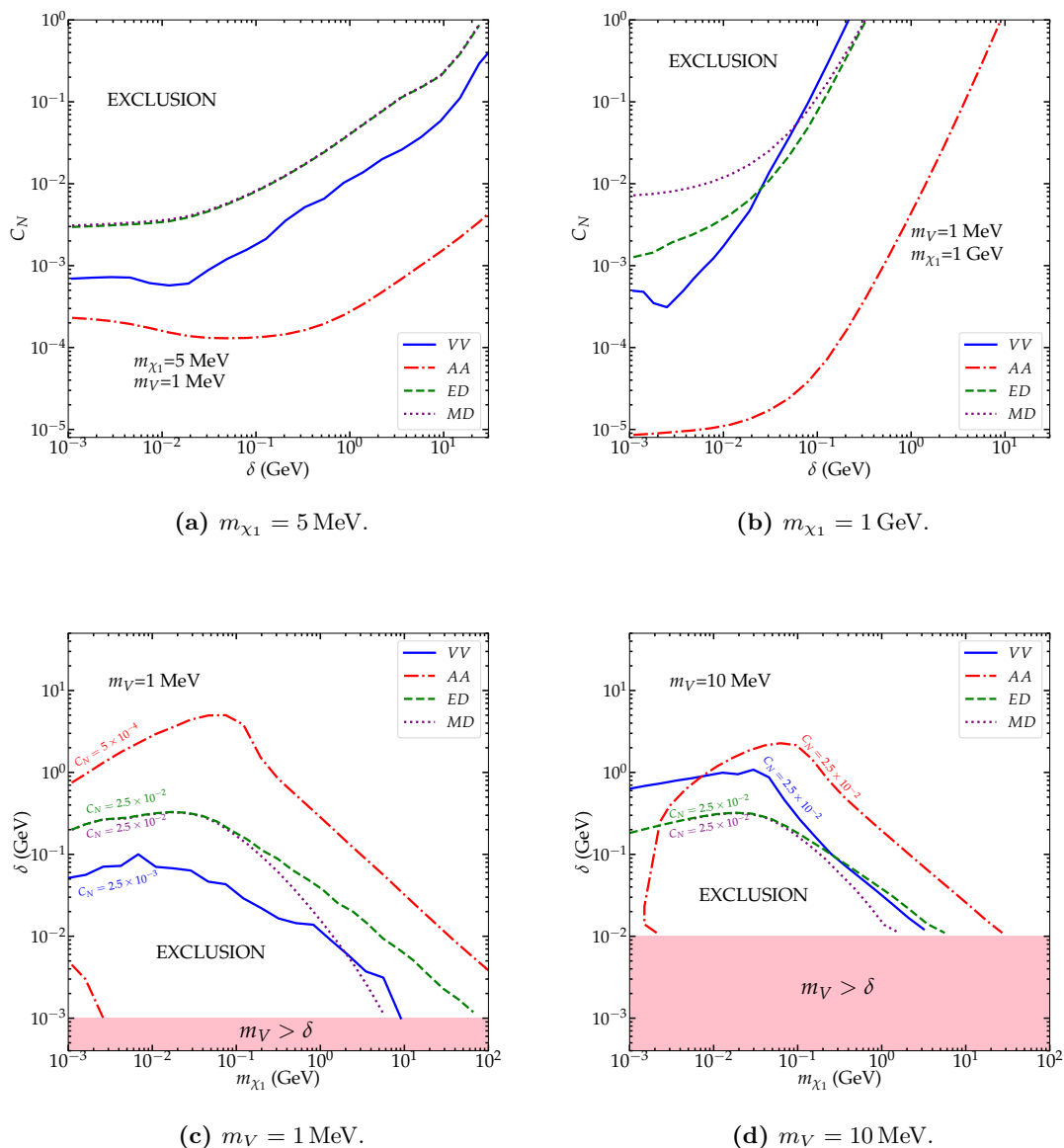
Figure 9. PandaX-4T limits are projected onto the plane $(\delta,\, C_N)$ [two upper panels] and the plane $(m_{\chi_1},\, \delta)$ [two lower panels]. The line-of-sight halo integration D_{eff} is taken as 1 kpc. The benchmark interactions are VV (blue solid lines), AA (red dash-dotted line), ED (green dashed line), and MD (purple dotted line). In panel (a), ED and MD lines overlap. We fixed $\Lambda_{E(M)} = 100\,\mathrm{MeV}$ for ED and MD.
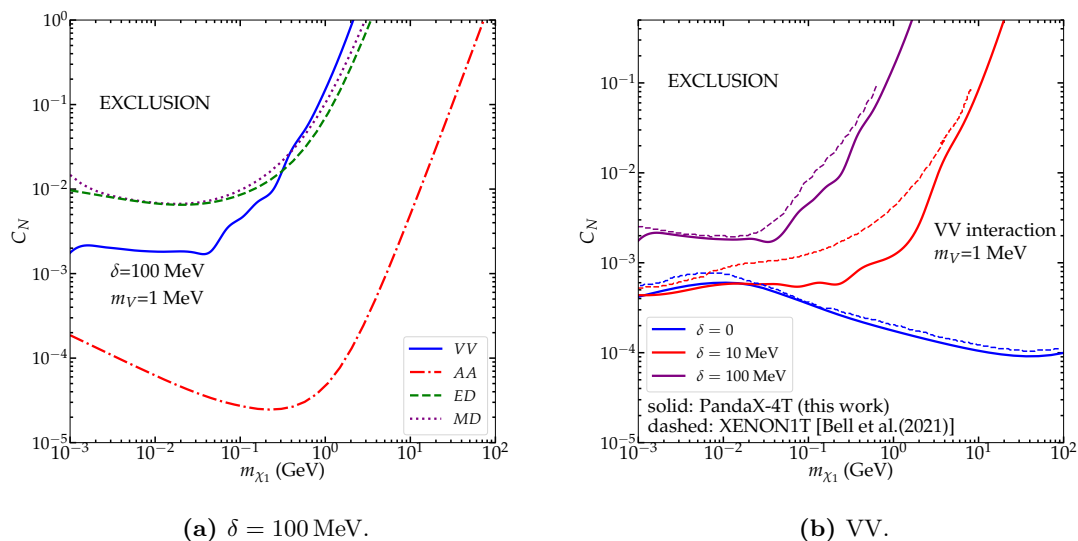
Figure 10. 95% upper limits projected in the (m_χ, C_N) plane. (a) the limits with fixed values $\delta = 100 \, \text{MeV}$ and $m_V = 1 \, \text{MeV}$ for VV, AA, ED, and MD. (b) Comparison between XENON1T and PandaX-4T based on the VV interaction. The XENON1T limit from ref. [29] is used for comparison.

region again for AA interaction. Thus, as long as we choose some stronger coupling, this allowed region can sink to the inaccessible (pink) region. In figure 9d, we take all the coupling strengths $C_N = 2.5 \times 10^{-2}$. A turning point then appears in all the interactions, and the limits behave differently at the smaller and larger m_{χ_1} regions. We can understand these points and limits as follows. The upper limits of δ at the large m_{χ_1} region decrease with respect to m_{χ_1}, mainly because DM number density ρ_0/m_{χ_1} decreases. The limits at the small m_{χ_1} region are similar to vDM limits, which always increase with m_{χ_1}. With heavy mediator masses $m_V = 10 \, \text{MeV}$ and $C_N = 2.5 \times 10^{-2}$, we find that PandaX-4T provides the most stringent limit for AA in the large m_{χ_1} region but for VV in the lower m_{χ_1} region. With the help of the CRDM scenario, the PandaX-4T exclusion of δ can be extended to $0.1 \, \text{GeV}$, even $1 \, \text{GeV}$ in some cases.

Finally, in figure 10, we present the 95% upper limits projected in the (m_χ, C_N) plane. The mediator mass and astrophysical effective length are fixed to $m_V = 1 \, \text{MeV}$ and $D_{\text{eff}} = 1 \, \text{kpc}$, respectively. In figure 10a, the upper limits of PandaX-4T are based on the scenarios: VV (blue solid line), AA (red dashed-dotted line), ED (green dashed line), and MD (purple dotted line). With the fixed values $\delta = 100 \, \text{MeV}$, the ordering of 95% limits in four scenarios remain similar to those in figure 9. In figure 10b, the previous XENON1T limits (dashed lines) are taken from ref. [29]. Because ref. [29] only considers the VV interaction, we use the same parameter configurations as theirs for a comparison between the elastic case (blue lines), $\delta = 10 \, \text{MeV}$ (red lines), and $\delta = 100 \, \text{MeV}$ (purple lines). Thus, the results of this study generally agree with the limits derived in ref. [29]. We also notice that the CRDM fluxes are roughly 10 orders of magnitudes lower than vDM, see figure 6a.

Because of the higher kinetic energy of CRDM, the PandaX-4T data can probe sub-GeV DM region in CRDM but not in vDM scheme. An example comparison is demonstrated in figure 12a of the appendix C.

5 Conclusion and prospect

In this study, we are motivated by the feature that DM relic density can be simply fulfilled at the co-annihilation region. However, the DM located in this region escapes from the standard DM direct detection constraints. Therefore, we investigated inelastic DM models that contain a pair of almost mass-degenerated DM particles χ_1 and χ_2. Because the standard DD method is not able to detect the vDM with extremely low momentum, this kind of inelastic DM model can be hidden within the analysis unless the DM mass is heavy enough $m_{\chi_1} \sim \mathcal{O}(\text{TeV})$. By considering the relativistic CRDM events created by the collision between the nonrelativistic vDM with the CR proton and helium, the lightest χ_1 can be excited to χ_2 and successively decay back to χ_1. Energetic χ_1 can be detected within the DM underground detector, such as PandaX-4T, in this study. *We have thus demonstrated that mass splitting $\delta < \mathcal{O}(1\,\text{GeV})$ can still be achieved with the DM mass range considered in this study with the latest PandaX-4T data, even though we conservatively take the astrophysical parameter $D_{\text{eff}} = 1$ kpc.*

Recently, a similar study [29] considered the VV interaction and produced a rather flat cross section with respect to the CR proton energy E_p. Beyond the scope of ref. [29], we also studied several different interactions, including both fermionic and scalar DM. By studying the predicted CRDM spectra of the different interactions, we found that the parameters (m_{χ_1}, δ, m_V, and E_p) play different roles in the fermionic AA interactions of eq. (2.2) compared with others, while the fermionic VV interaction of eq. (2.2) is almost identical with the scalar interaction of eq. (2.4). Conversely, we also studied the dimension-suppressed dipole-like interactions of eq. (2.3) and eq. (2.5). Because χ_1 can be relativistic before colliding with xenon in the detectors, we used the velocity-dependent form factor based on the effective theory framework. Therefore, our results for AA and dipole-like interactions are more reliable.

We then comment on possible constraints from other experiments that may be able to test the same parameter space. We focused on the mass of mediator m_V smaller than δ and m_{χ_1} in this study. Then, we assumed that the mediator is leptophobic. With these two conditions, the cross sections of DM production via off-shell mediators in fixed targets, B-factories, and LHC experiments are suppressed. Therefore, if $C_N \lesssim 10^{-2}$, we can safely ignore the above constraints in our scenarios.[3] However, the light leptophobic mediator is confronted with the constraints of low-energy n-Pb scattering [47, 48] and hadronic $\Upsilon(1S)$ decay [52]. In particular, the former provides the constraint $C_N \lesssim 5 \times 10^{-3}$ for $m_V \lesssim 10\,\text{MeV}$ [53] but loses its exclusion power when m_V increases. We find that the upper limit of C_N from the low energy n-Pb scattering can be complemented to the PandaX-4T limit derived in this study. For a comparison, one can refer to appendix C for more details. More constraints and searches for light mediator V can be found in refs. [53–55].

---

[3]Note that this mass spectrum setting is different from the usual ones with $m_V > 2m_{\chi_1} + \delta$ in refs. [49–51].

In the last paragraph, we would like to note several interesting extensions of this study, even though they are beyond the scope of this study. Interesting follow-up research should consider the Earth's attenuation effect of CRDM propagation. In this study, we only focused on the exclusion limit, but the attenuation can be important when the $\chi_1 p$ interaction cross section is large. Compared with the scenario for elastic CRDM scattering with Earth atoms, the inelastic scattering requires two dark particle propagation equations. In addition, the geometry of the propagation region might be complicated, and it can be challenging to solve the propagation equations analytically. Thus, we plan to return to this issue in the future with a numerical solution. Another interesting follow-up study would describe the form factor more precisely. In this study, we simply rescaled the form factor obtained by the assumption of elastic scattering. In addition, only the leading order of the velocity contribution has been included. Although much effort may be needed, this research would be useful, particularly if a more realistic form factor was developed for inelastic scattering.

Acknowledgments

A Kinematics of two-body inelastic collisions

As schematically shown in figure 1, there are two scenarios of DM collisions: (i) the high-energy protons of cosmic rays scattering with stationary DM χ, namely, $p + \chi_1 \to p' + \chi_2$, where χ_2 is the excited state of χ_1 with a mass of $m_{\chi_2} = m_{\chi_1} + \delta$; (ii) the accelerated DM colliding with the stationary nucleus N in the detector $\chi_1 + N \to \chi_2 + N'$.

Considering the general two-body relativistic collision, $p_1 + p_2 \to p_3 + p_4$, their masses are m_i with $i = 1, 2, 3, 4$. We can write down the 4-momentum of each particle of the process in lab frame Σ^L:

$$
\begin{aligned}
p_1 &= (E_1, \mathbf{p}_1), \\
p_2 &= (E_2 = m_2, \mathbf{p}_2 \simeq 0), \\
p_3 &= (E_3, \mathbf{p}_3), \\
p_4 &= (E_4, \mathbf{p}_4).
\end{aligned}
\tag{A.1}
$$

In the center-of-mass (CM) frame Σ^*, all physical quantities are marked with $*$:

$$
\begin{aligned}
p_1^* &= (E_1^*, \mathbf{p}_1^*), \\
p_2^* &= (E_2^*, \mathbf{p}_2^* = -\mathbf{p}_1^*), \\
p_3^* &= (E_3^*, \mathbf{p}_3^*), \\
p_4^* &= (E_4^*, \mathbf{p}_4^* = -\mathbf{p}_3^*),
\end{aligned}
\tag{A.2}
$$

The total 4-momentum P of two systems are simply:

$$P(\Sigma^*) = (M, 0), \quad \text{and} \quad P(\Sigma^L) = (E_1 + m_2, \mathbf{p}_1). \tag{A.3}$$

Also:

$$|\mathbf{p}_3^*| = \frac{1}{2}\sqrt{\frac{(m_3^2 - m_4^2)^2}{M^2} + M^2 - 2(m_3^2 + m_4^2)}, \quad \text{and}$$
$$E_4^* = \frac{M^2 - m_3^2 + m_4^2}{2M}. \tag{A.4}$$

Boosting from the CM frame to the lab frame, one will obtain the magnitude of velocity $\beta = |\mathbf{p}_1| / (E_1 + m_2)$ and Lorentz factor $\gamma = (E_1 + m_2)/M$. Therefore, the invariant mass M will be related to E_1 via:

$$M = (E_1 + m_2)\sqrt{1 - \beta^2} = \sqrt{m_2^2 + m_1^2 + 2m_2 E_1}. \tag{A.5}$$

A.1 Accelerating process $p + \chi_1 \rightarrow p' + \chi_2$

In the process of $p(p_1) + \chi_1(p_2) \rightarrow p'(p_3) + \chi_2(p_4)$, where the four-momentum label has been given in parentheses, one has $p_2 = (E_2 = m_{\chi_1}, \mathbf{p}_2 \simeq 0)$, and χ_2 is the accelerated DM after collision, with energy E_4. We can insert $E_1 = E_p$, $m_1 = m_3 = m_p$, $m_2 = m_{\chi_1}$, and $m_4 = m_{\chi_1} + \delta$ into eq. (A.4) and obtain:

$$E_4^* = E_{\chi_2}^* = \frac{m_{\chi_1}(m_{\chi_1} + E_p) + \delta(\delta/2 + m_{\chi_1})}{M}. \tag{A.6}$$

If $\delta = 0$, we can safely return to the case of elastic collision. Also, the condition $E_{\chi_2}^* > (m_{\chi_1} + \delta)$ is required for χ_1 being excited to χ_2. This results in a universal lower limit for E_p, which is $m_p + \delta + \frac{\delta(\delta + 2m_p)}{2m_{\chi_1}}$.

To determine the minimum value of E_p in eq. (3.9), it would be useful to introduce the scattering angle θ^* where the component of $\mathbf{p}_3^*$ along the direction of $\mathbf{p}_1^*$ is $|\mathbf{p}_3^*|\cos\theta^*$. Therefore, we substitute E_4 by $T_{\chi_2} + m_{\chi_1} + \delta$ to obtain:

$$T_{\chi_2} = \frac{E_{\chi_2}^*(m_{\chi_1} + E_p) - |\mathbf{p}_{\chi_2}^*|\sqrt{E_p^2 - m_p^2}\cos\theta^*}{\sqrt{(m_{\chi_1} + m_p)^2 + 2m_{\chi_1}(E_p - m_p)}} - (m_{\chi_1} + \delta). \tag{A.7}$$

where $|\mathbf{p}_{\chi_2}^*| = \sqrt{(E_{\chi_2}^*)^2 - (m_{\chi_1} + \delta)^2}$.

We would like to obtain the range of E_p from eq. (A.7). Because $T_{\chi_2}(E_p, \cos\theta^*)$ reaches maximum and minimum values when $\theta^* = \pi$ and $\theta^* = 0$, respectively, we may define $T_{\chi_2}^{\max}(E_p) = T_{\chi_2}(E_P, \theta^* = \pi)$ and $T_{\chi_2}^{\min}(E_p) = T_{\chi_2}(E_P, \theta^* = 0)$. For a fixed E_p, the allowed region of T_{χ_2} should be between $T_{\chi_2}^{\min}$ and $T_{\chi_2}^{\max}$, illustrated in figure 11.

Similar to the elastic case, the constraint of T_{χ_2} can be expressed by $E_p^{\min}(T_{\chi_2})$:

$$E_p > E_p^{\min} = \frac{T_{\chi_2} + \delta}{2} + \sqrt{\frac{T_{\chi_2}(m_{\chi_1} + \frac{T_{\chi_2}}{2} + \delta)(2m_p^2 + m_{\chi_1}T_{\chi_2} - \frac{\delta^2}{2})}{2m_{\chi_1}T_{\chi_2} - \delta^2}}. \tag{A.8}$$

where $2m_{\chi_1}T_{\chi_2} > \delta^2$ should be satisfied. The minimum value of $E_p^{\min}$ is $m_p + \delta + \frac{\delta(\delta + 2m_p)}{2m_{\chi_1}}$. The condition $E_p > E_p^{\min}(T_{\chi_2})$ is equivalent to $T_{\chi_2}^{\min}(E_p) < T_{\chi_2} < T_{\chi_2}^{\max}(E_p)$.
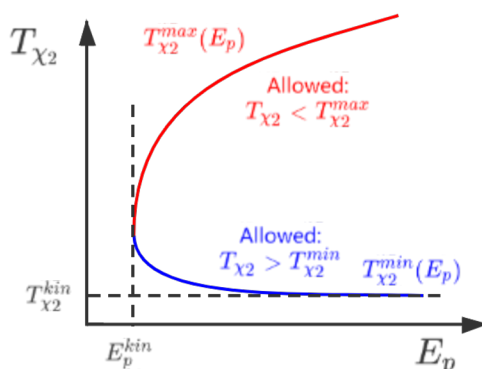
Figure 11. Kinetic relation between incoming E_p and outgoing T_{χ_2}. From eq. (A.7), the red curve represents $T_{\chi_2}^{\max}$ with $\theta^* = \pi$, and the blue curve represents $T_{\chi_2}^{\min}$ with $\theta^* = 0$. The kinetic allowed region is between the red and blue curves. The two curves can be uniformly described by eq. (A.8). Two limits of the curve correspond to two kinematic constraints for inelastic collision: $T_{\chi_2}^{kin} = \frac{\delta^2}{2m_{\chi_1}}$ and $E_p^{kin} = m_p + \delta + \frac{\delta(\delta + 2m_p)}{2m_{\chi_1}}$.

A.2 Process in the detector $\chi_1 + N \to \chi_2 + N'$

For the process $\chi_1(p_1) + N(p_2) \to \chi_2(p_3) + N'(p_4)$ with $p_2 = (E_2 = m_N, \mathbf{p}_2 \simeq 0)$, we can swap the index that the incoming particle 1 is inelastic DM, but E_4 is the energy of the heavy nucleus after the collision. By taking the masses $m_2 = m_4 = m_N$, $m_1 = m_{\chi_1}$, and $m_3 = m_{\chi_1} + \delta$, we can rewrite eq. (A.4) as:

$$E_4^* = E_{N'}^* = \frac{m_N(m_N + E_\chi) - \delta(\delta/2 + m_{\chi_1})}{M}. \tag{A.9}$$

We can boost eq. (A.9) from the CM frame to the Lab frame to obtain the recoil energy $Q = E_4 - m_N$ of nucleus. Finally, the minimal kinetic energy required to obtain a specific recoil energy Q is:

$$T_\chi^{\min} = \frac{Q}{2} - m_{\chi_1} + \frac{\delta(m_{\chi_1} + \delta/2)}{2m_N}$$
$$+ \frac{\sqrt{Q(2m_N + Q)(m_N Q + \delta^2/2)(m_N Q + (2m_{\chi_1} + \delta)^2/2)}}{2m_N Q}. \tag{A.10}$$

B Scattering cross sections

B.1 $2 \to 3$ cross sections

The differential cross section for the inelastic scattering $p(p_1)\chi_1(p_2) \to p'(k_1)\chi_1(k_2)V(k_3)$ can be represented as:

$$d\sigma_{p\chi_1 \to p'\chi_1 V} = \frac{(2\pi)^4 |\mathcal{M}_{2\to 3}|^2}{4\sqrt{(p_1 \cdot p_2)^2 - m_p^2 m_{\chi_1}^2}} d\phi_3(p_1 + p_2; k_1, k_2, k_3), \tag{B.1}$$

where $\mathcal{M}_{2\to3}$ is the total scattering amplitude, and $\phi_3(p_1 + p_2; k_1, k_2, k_3)$ is the three-body phase space. Using the recursive relation, we have:

$$d\phi_3(p_1 + p_2; k_1, k_2, k_3) = d\phi_2(p_1 + p_2; k_1, q) \times d\phi_2(q; k_2, k_3)(2\pi)^3 dq^2 \tag{B.2}$$

where q is the four-momentum of χ_2. This kind of technique is extensively used in ref. [56] With the narrow width approximation, which corresponds to the case of on-shell χ_2, we can separate the scattering process into collision and decay parts, namely, $p\chi_1 \to p'\chi_2$ and $\chi_2 \to \chi_1 V$. Then, $|\mathcal{M}_{2\to3}|^2$ can be written as:

$$|\mathcal{M}_{2\to3}|^2 = |\mathcal{M}_{2\to2}|^2 \frac{\pi\delta(q^2 - m_{\chi_2}^2)}{m_{\chi_2}\Gamma_{\chi_2}}|\mathcal{M}_{1\to2}|^2, \tag{B.3}$$

where $\mathcal{M}_{2\to2}$ is the scattering amplitude of the collision part, and $\mathcal{M}_{1\to2}$ is that of the decay part.

We can decompose the total differential cross in the following form:

$$d\sigma_{p\chi_1 \to p'\chi_1 V} = d\sigma_{p\chi_1 \to p'\chi_2} dB_{\chi_2 \to \chi_1 V}, \tag{B.4}$$

where we have:

$$d\sigma_{p\chi_1 \to p'\chi_2} = \frac{(2\pi)^4|\mathcal{M}_{2\to2}|^2}{4\sqrt{(p_1 \cdot p_2)^2 - m_p^2 m_{\chi_1}^2}} d\phi_2(p_1 + p_2; k_1, q), \tag{B.5}$$

And:

$$\begin{aligned} dB_{\chi_2 \to \chi_1 X} &= \frac{2\pi}{\Gamma_{\chi_2}}\delta(q^2 - m_{\chi_2}^2)\frac{|\mathcal{M}_{1\to2}|^2}{2m_{\chi_2}}d\phi_2(q; k_2, k_3)(2\pi)^3 dq^2 \\ &= \frac{d\Gamma_{\chi_2 \to \chi_1 V}}{\Gamma_{\chi_2}}\delta(q^2 - m_{\chi_2}^2)dq^2. \end{aligned} \tag{B.6}$$

The total width of χ_2 is defined as Γ_{χ_2}.

Finally, we successfully obtain the total differential cross section as eq. (3.12):

$$\frac{d\sigma_{p\chi_1 \to p'\chi_1 V}}{dT_{\chi_1}} = \int \frac{d\sigma_{p\chi_1 \to p'\chi_2}}{dT_{\chi_2}}\frac{dT_{\chi_2}}{dT_{\chi_1}}\frac{dB_{\chi_2 \to \chi_1 V}}{d\cos\theta'}d\cos\theta', \tag{B.7}$$

where θ' is the angle of χ_1 in the χ_2 rest frame. In this frame:

$$\frac{d\Gamma_{\chi_2 \to \chi_1 V}}{d\Omega'} = \frac{|p_{\chi_1}^*|}{32\pi^2 q^2}|\mathcal{M}_{1\to2}|^2 \tag{B.8}$$

where Ω' is the solid angle. In the presence of vector and axial vector interactions, we can prove that $|\mathcal{M}_{1\to2}|^2$ is independent of the angle. Then, the aforementioned θ' can be chosen as the angle formed by χ_2 momentum in the lab frame of $p\chi_1$ and χ_1 momentum for $\chi_2 \to \chi_1 V$ decay in the χ_2 rest frame. Therefore:

$$dB_{\chi_2 \to \chi_1 V} = \frac{d\Gamma_{\chi_2 \to \chi_1 V}}{\int d\Gamma_{\chi_2 \to \chi_1 V}}\delta(q^2 - m_{\chi_2}^2)dq^2 \longrightarrow \frac{d\Omega'}{4\pi} \tag{B.9}$$

Ultimately, the factor of $\delta(q^2 - m_{\chi_2}^2)dq^2$ will drop out in the process of integration over the three-body phase space [57, 58]. A trivial integration over $d\phi'$ gives the $dB_{\chi_2 \to \chi_1 V}/d\cos\theta' = 1/2$.

B.2 $2 \to 2$ cross sections

B.2.1 The accelerating process $p + \chi_1 \to p' + \chi_2$

To calculate the total differential cross section between cosmic ray protons and inelastic dark matter in eq. (B.7), we must derive $d\sigma_{p\chi_1 \to p'\chi_2}/dT_{\chi_2}$ first:

$$\frac{d\sigma_{p\chi_1 \to p'\chi_2}}{dT_{\chi_2}} = \frac{d\sigma_{p\chi_1 \to p'\chi_2}}{dt}\left|\frac{dt}{dT_{\chi_2}}\right| = \frac{\overline{|\mathcal{M}|^2}}{16\pi\lambda(s, m_p^2, m_{\chi_1}^2)}\left|\frac{dt}{dT_{\chi_2}}\right| \tag{B.10}$$

where $\overline{|\mathcal{M}|^2} = \sum_{\text{spins}} |\mathcal{M}|^2/4$ is the proton-DM scattering matrix element squared, averaged over initial spins and summed over final spins. We define the Kallen function as $\lambda(x, y, z) = (x - y - z)^2 - 4yz$, and the Mandelstam variables are:

$$\begin{aligned}
s &= m_{\chi_1}^2 + m_p^2 + 2m_{\chi_1}E_p, \\
t &= -2m_{\chi_1}T_{\chi_2} + \delta^2, \\
u &= m_p^2 + m_{\chi_1}^2 - 2m_{\chi_1}(E_p - T_{\chi_2} - \delta).
\end{aligned} \tag{B.11}$$

The amplitude squared $|\mathcal{M}_{ij}|^2$ with i for the VNN interaction type and j for the $V\chi\chi$ interaction type are given below.

For fermionic DM:

- Vector-Vector interaction:

$$\begin{aligned}
\overline{|\mathcal{M}_{\text{VV}}|^2} = &\left[\frac{4(C_N^v)^2(C_\chi^v)^2 m_{\chi_1}}{\left(2m_{\chi_1}T_{\chi_2} + m_V^2 - \delta^2\right)^2}\right] \times \Big[-4m_{\chi_1}E_p\left(\delta + T_{\chi_2}\right) + 4m_{\chi_1}E_p{}^2 \\
&-2T_{\chi_2}\left(m_p^2 + m_{\chi_1}\left(m_{\chi_1} - T_{\chi_2}\right)\right) + \delta^2\left(m_{\chi_1} - T_{\chi_2}\right)\Big].
\end{aligned} \tag{B.12}$$

- Axial vector-Axial vector interaction:

$$\begin{aligned}
\overline{|\mathcal{M}_{\text{AA}}|^2} = &\left[\frac{4(C_N^a)^2(C_\chi^a)^2 m_{\chi_1}}{\left(2m_{\chi_1}T_{\chi_2} + m_V^2 - \delta^2\right)^2}\right] \times \Big[-4m_{\chi_1}E_p\left(\delta + T_{\chi_2}\right) + 4m_{\chi_1}E_p^2 \\
&+2m_p^2\left(4\delta + T_{\chi_2}\right) + 8m_p^2 m_{\chi_1} + m_{\chi_1}\left(-\delta^2 + 4\delta T_{\chi_2} + 2T_{\chi_2}^2\right) \\
&+2m_{\chi_1}^2 T_{\chi_2} + \delta^2\left(-\left(2\delta + T_{\chi_2}\right)\right) \\
&+(2m_p^2 T_{\chi_2}\left(\delta + 2m_{\chi_1}\right)^2\left(-\delta^2 + 2m_{\chi_1}T_{\chi_2} + 2m_V^2\right))/m_V^4\Big].
\end{aligned} \tag{B.13}$$

- Vector-Magnetic Dipole interaction:

$$\begin{aligned}
\overline{|\mathcal{M}_{\text{MD}}|^2} = &\left[\frac{4(C_N^v)^2 m_{\chi_1}/(\Lambda_M)^2}{\left(2m_{\chi_1}T_{\chi_2} + m_V^2 - \delta^2\right)^2}\right] \times 4\Big[4m_{\chi_1}E_p^2\left(2m_{\chi_1}T_{\chi_2} - \delta^2\right) \\
&-4m_{\chi_1}E_p\left(\delta + T_{\chi_2}\right)\left(2m_{\chi_1}T_{\chi_2} - \delta^2\right) \\
&-2m_p^2 T_{\chi_2}\left(\delta + 2m_{\chi_1}\right)^2 + \left(2m_{\chi_1}T_{\chi_2} - \delta^2\right) \\
&\times \left(\delta^2\left(m_{\chi_1} + T_{\chi_2}\right) + 4\delta m_{\chi_1}T_{\chi_2} + 2m_{\chi_1}^2 T_{\chi_2}\right)\Big].
\end{aligned} \tag{B.14}$$

- Vector-Electric Dipole interaction:

$$\overline{|\mathcal{M}_{\text{ED}}|^2} = \left[\frac{4(C_N^v)^2 m_{\chi_1}/(\Lambda_E)^2}{(2m_{\chi_1} T_{\chi_2} + m_V^2 - \delta^2)^2} \right] \times 4\Big[4m_{\chi_1} E_p{}^2 \left(2m_{\chi_1} T_{\chi_2} - \delta^2\right)$$
$$-4m_{\chi_1} E_p \left(\delta + T_{\chi_2}\right) \left(2m_{\chi_1} T_{\chi_2} - \delta^2\right)$$
$$-\delta^2 m_{\chi_1} \left(3\delta^2 + 4m_p^2 - 4\delta T_{\chi_2} - 2T_{\chi_2}^2\right)$$
$$-\delta^2 \left(\delta^2 + 2m_p^2\right) \left(2\delta + T_{\chi_2}\right) + 8\delta^2 m_{\chi_1}^2 T_{\chi_2} - 4m_{\chi_1}^3 T_{\chi_2}^2\Big]. \tag{B.15}$$

For scalar DM:

- Combining the vector interaction for SM and $\mathcal{L}_1^s$ in eq. (2.4) for scalar DM yields:

$$\overline{|\mathcal{M}|^2} = \left[\frac{4(C_N^v)^2 (g_\chi)^2 m_{\chi_1}}{(2m_{\chi_1} T_{\chi_2} + m_V^2 - \delta^2)^2} \right]$$
$$\times \Big[m_{\chi_1} \left(4E_p{}^2 + \delta^2 - 4E_p\left(\delta + T_{\chi_2}\right) - 2m_{\chi_1} T_{\chi_2}\right) \Big]. \tag{B.16}$$

- Combining the vector interaction for SM and $\mathcal{L}_2^s$ in eq. (2.5) for scalar DM yields:

$$\overline{|\mathcal{M}|^2} = \left[\frac{4(C_N^v)^2 m_{\chi_1}/(\Lambda_s)^4}{(2m_{\chi_1} T_{\chi_2} + m_V^2 - \delta^2)^2} \right] \tag{B.17}$$
$$\times \frac{1}{4}\Big[m_{\chi_1} \left(4E_p{}^2 + \delta^2 - 4E_p\left(\delta + T_{\chi_2}\right) - 2m_{\chi_1} T_{\chi_2}\right) \left(2m_{\chi_1} T_{\chi_2} - \delta^2\right)^2 \Big].$$

The corresponding differential cross section can be written as:

$$\frac{d\sigma_{p\chi_1 \to p'\chi_2}}{dT_{\chi_2}} = \frac{m_{\chi_1}}{8\pi\lambda(s, m_p^2, m_{\chi_1}^2)} \overline{|\mathcal{M}|^2} \tag{B.18}$$

B.2.2 Process in the detector $\chi_1 + N \to \chi_2 + N'$

Similarly, we can derive $d\sigma_{\chi N}/dQ$ of eq. (3.16). To calculate $\overline{|\mathcal{M}|^2}$, we must only change the Mandelstam variables as:

$$s = m_{\chi_1}^2 + m_N^2 + 2m_N(T_{\chi_1} + m_{\chi_1}),$$
$$t = -2m_N Q,$$
$$u = (m_N - m_{\chi_1})^2 + 2m_N(Q - T_{\chi_1}) + \delta(2m_{\chi_1} + \delta). \tag{B.19}$$

The amplitude squared $|\mathcal{M}_{ij}|^2$ with i for the Vpp interaction type and j for the $V\chi\chi$ interaction type are given below.

For fermionic DM:

- Vector-Vector interaction:

$$\overline{|\mathcal{M}_{\text{VV}}|^2} = \left[\frac{4(C_N^v)^2 (C_\chi^v)^2 m_N}{(2Qm_N + m_V^2)^2} \right] \times \Big[m_N \left(-\delta^2 - 4\left(m_{\chi_1} + T_{\chi_1}\right)\left(-m_{\chi_1} + Q - T_{\chi_1}\right) + 2Q^2\right)$$
$$-2Qm_N^2 - 2m_{\chi_1}\left(\delta^2 + m_{\chi_1}(2\delta + Q)\right) - 2\delta T_{\chi_1}\left(\delta + 2m_{\chi_1}\right) + \delta^2 Q\Big] \tag{B.20}$$

- Axial vector-Axial vector interaction:

$$\overline{|\mathcal{M}_{\mathrm{AA}}|^2} = \left[\frac{4(C_N^a)^2(C_\chi^a)^2 m_N}{(2Qm_N + m_V^2)^2}\right] \tag{B.21}$$
$$\times \Big[m_N \left(\delta^2 + m_{\chi 1}\left(8\delta - 4Q + 8T_{\chi 1}\right) + 12m_{\chi 1}^2 + 2Q^2 + 4T_{\chi 1}\left(T_{\chi 1} - Q\right)\right)$$
$$+ 2Qm_N^2 + 2m_{\chi 1}^2(Q - 2\delta) - 2\delta m_{\chi 1}\left(\delta - 2Q + 2T_{\chi 1}\right) + \delta^2\left(Q - 2T_{\chi 1}\right)$$
$$+ \left(2m_N\left(\delta + 2m_{\chi 1}\right)^2\left(2Q^2 m_N^2 + Qm_N\left(\delta^2 + 2m_V^2\right) + \delta^2 m_V^2\right)\right)/m_V^4 \Big].$$

- Vector-Magnetic Dipole interaction:

$$\overline{|\mathcal{M}_{\mathrm{MD}}|^2} = \left[\frac{4(C_N^v)^2 m_N/(\Lambda_M)^2}{(2Qm_N + m_V^2)^2}\right] \times 4\Big[4m_N m_{\chi 1}^2\left(-\delta^2 + Q^2 - 2\delta Q\right) \tag{B.22}$$
$$-\delta^2 m_N\left(\delta^2 - 2Q^2 + 4QT_{\chi 1}\right) - 4\delta m_N m_{\chi 1}\left(\delta^2 - 2Q^2 + \delta Q + 2QT_{\chi 1}\right)$$
$$+\delta^2 Q\left(\delta + 2m_{\chi 1}\right)^2 - 2Qm_N^2\left(\delta^2 + 4m_{\chi 1}\left(\delta + Q - 2T_{\chi 1}\right) + 4QT_{\chi 1} - 4T_{\chi 1}^2\right)\Big].$$

- Vector-Electric Dipole interaction:

$$\overline{|\mathcal{M}_{\mathrm{ED}}|^2} = \left[\frac{4(C_N^v)^2 m_N/(\Lambda_E)^2}{(2Qm_N + m_V^2)^2}\right] \times 4\Big[-\delta^2 m_N\left(\delta^2 - 2Q^2 + 4QT_{\chi 1}\right) - 4m_N m_{\chi 1}^2(\delta + Q)^2$$
$$-4\delta m_N m_{\chi 1}\left(\delta^2 + \delta Q + 2QT_{\chi 1}\right) + \delta^2 Q\left(\delta + 2m_{\chi 1}\right)^2$$
$$-2Qm_N^2\left(\delta^2 + 4m_{\chi 1}\left(Q - 2T_{\chi 1}\right) - 4m_{\chi 1}^2 + 4QT_{\chi 1} - 4T_{\chi 1}^2\right)\Big]. \tag{B.23}$$

For scalar DM:

- Combining the vector interaction for SM and $\mathcal{L}_1^s$ in eq. (2.4) for scalar DM yields:

$$\overline{|\mathcal{M}|^2} = \left[\frac{4(C_N^v)^2(g_\chi)^2 m_N}{(2Qm_N + m_V^2)^2}\right] \times 2\Big[m_{\chi 1}^2\left(-2\delta + 2m_N - Q\right) \tag{B.24}$$
$$+ m_{\chi 1}\left(-\delta^2 - 2Qm_N + 2T_{\chi 1}\left(2m_N - \delta\right)\right) + T_{\chi 1}\left(2m_N\left(T_{\chi 1} - Q\right) - \delta^2\right)\Big].$$

- Combining the vector interaction for SM and $\mathcal{L}_2^s$ in eq. (2.5) for scalar DM yields:

$$\overline{|\mathcal{M}|^2} = \left[\frac{4(C_N^v)^2 m_N/(\Lambda_s)^4}{(2Qm_N + m_V^2)^2}\right] \times 2Q^2 m_N^2\Big[2m_N\left(m_{\chi 1} + T_{\chi 1}\right)\left(m_{\chi 1} - Q + T_{\chi 1}\right)$$
$$-m_{\chi 1}^2(2\delta + Q) - \delta m_{\chi 1}\left(\delta + 2T_{\chi 1}\right) - \delta^2 T_{\chi 1}\Big]. \tag{B.25}$$

Again, the corresponding differential cross section is

$$\frac{d\sigma_{\chi N}}{dQ} = \frac{m_N}{8\pi\lambda(s, m_{\chi 1}^2, m_N^2)}\overline{|\mathcal{M}|^2}. \tag{B.26}$$
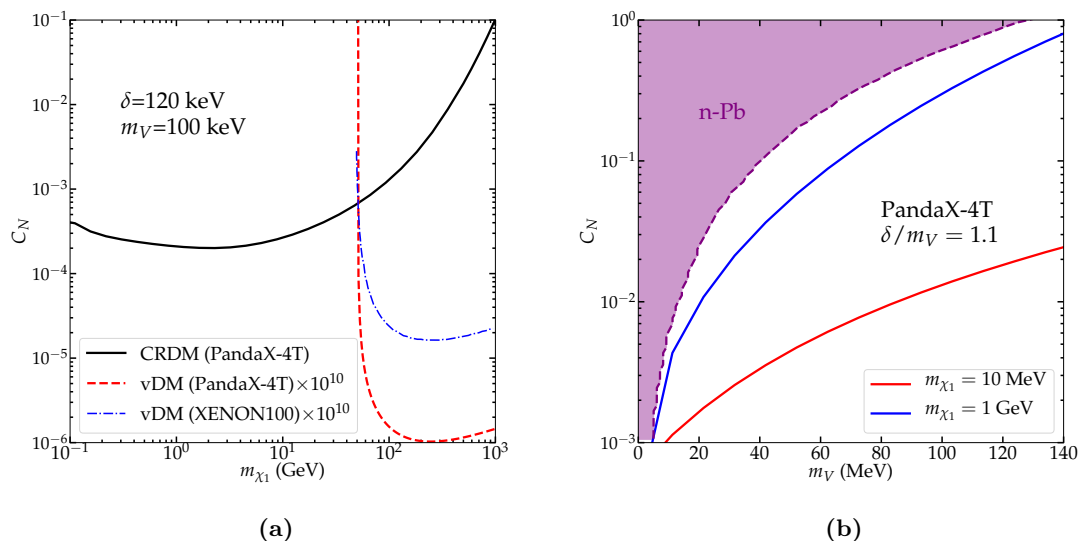
Figure 12. The 95% C.L. of PandaX-4T for both vDM (red dashed line) and CRDM (black solid line) in figure 12a. As a comparison, we translate the XENON100 95% limit [59] for vDM (blue dash-dotted line). We scale vDM limit with a factor 10^{10} in order to compare it with CRDM in a same range. The mass splitting and mediator mass are taken as $\delta = 120\,\text{keV}$ and $m_V = 100\,\text{keV}$. Figure 12b: the comparison to the previous n-Pb scattering limits [53] in the (m_V, C_N) plane. The purple region is the exclusion of n-Pb scattering experiment while the PandaX-4T CRDM limits are presented by blue line (1 GeV) and red line (10 MeV). With $\delta = 1.1 \times m_V$, the limits of CRDM detection are more stringent than the previous n-Pb scattering experiment.

C   Supplemental figures

In this section, we compare the new limits derived in this work with previous constraints, to demonstrate the advantage of CRDM for inelastic DM study.

In figure 12a, we compare the 95% limits between vDM (dashed and dash-dotted) and CRDM (solid) scheme in (C_N, m_{χ_1}) plane. Since the recoil energy of underground detectors can only reach $\delta \approx O(100\,\text{keV})$, we fix $\delta = 120\,\text{keV}$ and $m_V = 100\,\text{keV}$. Although the vDM limits are generally about 10 orders of magnitudes stronger than CRDM limits, they cannot probe the region $m_{\chi_1} \lesssim 50\,\text{GeV}$. Reversely, the CRDM limits can explore the parameter space for DM with a mass less than 50 GeV. We also translate the XENON100 limit from ref. [59] as a comparison. Similar constraints for inelastic vDM scheme can be found in refs. [60, 61].

In figure 12b, we show the upper limit of C_N in a function of m_V from n-Pb scattering (dashed purple) and our PandaX-4T CRDM limits (solid). We set $\delta = 1.1 \times m_V$ as a demonstration. The most stringent constraint for $m_V \lesssim 100\,\text{MeV}$ is derived from n-Pb scattering [47, 48, 53]. However, the CRDM limits can be still more stringent than the previous n-Pb scattering experiment, even if taking $m_{\chi_1} = 1\,\text{GeV}$.

References

[1] PLANCK collaboration, *Planck* 2018 *results. X. Constraints on inflation*, *Astron. Astrophys.* **641** (2020) A10 [`arXiv:1807.06211`] [INSPIRE].

[2] ATLAS collaboration, *Search for dark matter produced in association with a Standard Model Higgs boson decaying into b-quarks using the full run* 2 *dataset from the ATLAS detector*, *JHEP* **11** (2021) 209 [`arXiv:2108.13391`] [INSPIRE].

[3] CMS collaboration, *Search for new particles in events with energetic jets and large missing transverse momentum in proton-proton collisions at* $\sqrt{s} = 13$ *TeV*, *JHEP* **11** (2021) 153 [`arXiv:2107.13021`] [INSPIRE].

[4] XENON collaboration, *Dark matter search results from a one ton-year exposure of XENON*1*T*, *Phys. Rev. Lett.* **121** (2018) 111302 [`arXiv:1805.12562`] [INSPIRE].

[5] PANDAX-4T collaboration, *Dark matter search results from the PandaX-4T commissioning run*, *Phys. Rev. Lett.* **127** (2021) 261802 [`arXiv:2107.13438`] [INSPIRE].

[6] K. Griest and D. Seckel, *Three exceptions in the calculation of relic abundances*, *Phys. Rev. D* **43** (1991) 3191 [INSPIRE].

[7] J. Edsjo and P. Gondolo, *Neutralino relic density including coannihilations*, *Phys. Rev. D* **56** (1997) 1879 [`hep-ph/9704361`] [INSPIRE].

[8] H. Baer, T. Krupovnickas, A. Mustafayev, E.-K. Park, S. Profumo and X. Tata, *Exploring the BWCA (Bino-Wino Co-Annihilation) scenario for neutralino dark matter*, *JHEP* **12** (2005) 011 [`hep-ph/0511034`] [INSPIRE].

[9] C. Cheung, L.J. Hall, D. Pinner and J.T. Ruderman, *Prospects and blind spots for neutralino dark matter*, *JHEP* **05** (2013) 100 [`arXiv:1211.4873`] [INSPIRE].

[10] N. Nagata, H. Otono and S. Shirai, *Probing bino-wino coannihilation at the LHC*, *JHEP* **10** (2015) 086 [`arXiv:1506.08206`] [INSPIRE].

[11] S. Banerjee, S. Matsumoto, K. Mukaida and Y.-L.S. Tsai, *WIMP dark matter in a well-tempered regime: a case study on singlet-doublets fermionic WIMP*, *JHEP* **11** (2016) 070 [`arXiv:1603.07387`] [INSPIRE].

[12] Y.-L.S. Tsai, V.Q. Tran and C.-T. Lu, *Confronting dark matter co-annihilation of inert two Higgs doublet model with a compressed mass spectrum*, *JHEP* **06** (2020) 033 [`arXiv:1912.08875`] [INSPIRE].

[13] K. Cheung, Y.-L.S. Tsai, P.-Y. Tseng, T.-C. Yuan and A. Zee, *Global study of the simplest scalar phantom dark matter model*, *JCAP* **10** (2012) 042 [`arXiv:1207.4930`] [INSPIRE].

[14] J.M. Cline, K. Kainulainen, P. Scott and C. Weniger, *Update on scalar singlet dark matter*, *Phys. Rev. D* **88** (2013) 055025 [*Erratum ibid.* **92** (2015) 039906] [`arXiv:1306.4710`] [INSPIRE].

[15] T. Lin, E.W. Kolb and L.-T. Wang, *Probing dark matter couplings to top and bottom quarks at the LHC*, *Phys. Rev. D* **88** (2013) 063510 [`arXiv:1303.6638`] [INSPIRE].

[16] GAMBIT collaboration, *Status of the scalar singlet dark matter model*, *Eur. Phys. J. C* **77** (2017) 568 [arXiv:1705.07931] [INSPIRE].

[17] S. Matsumoto, Y.-L.S. Tsai and P.-Y. Tseng, *Light fermionic WIMP dark matter with light scalar mediator*, *JHEP* **07** (2019) 050 [arXiv:1811.03292] [INSPIRE].

[18] G. Arcadi, A. Djouadi and M. Raidal, *Dark matter through the Higgs portal*, *Phys. Rept.* **842** (2020) 1 [arXiv:1903.03616] [INSPIRE].

[19] LUX collaboration, *Results from a search for dark matter in the complete LUX exposure*, *Phys. Rev. Lett.* **118** (2017) 021303 [arXiv:1608.07648] [INSPIRE].

[20] PANDAX-II collaboration, *Exploring the dark matter inelastic frontier with* 79.6 *days of PandaX-II data*, *Phys. Rev. D* **96** (2017) 102007 [arXiv:1708.05825] [INSPIRE].

[21] T. Bringmann and M. Pospelov, *Novel direct detection constraints on light dark matter*, *Phys. Rev. Lett.* **122** (2019) 171801 [arXiv:1810.10543] [INSPIRE].

[22] Y. Ema, F. Sala and R. Sato, *Light dark matter at neutrino experiments*, *Phys. Rev. Lett.* **122** (2019) 181802 [arXiv:1811.00520] [INSPIRE].

[23] C.V. Cappiello, K.C.Y. Ng and J.F. Beacom, *Reverse direct detection: cosmic ray scattering with light dark matter*, *Phys. Rev. D* **99** (2019) 063004 [arXiv:1810.07705] [INSPIRE].

[24] C.V. Cappiello and J.F. Beacom, *Strong new limits on light dark matter from neutrino experiments*, *Phys. Rev. D* **100** (2019) 103011 [*Erratum ibid.* **104** (2021) 069901] [arXiv:1906.11283] [INSPIRE].

[25] W. Wang, L. Wu, J.M. Yang, H. Zhou and B. Zhu, *Cosmic ray boosted sub-GeV gravitationally interacting dark matter in direct detection*, *JHEP* **12** (2020) 072 [*Erratum ibid.* **02** (2021) 052] [arXiv:1912.09904] [INSPIRE].

[26] G. Guo, Y.-L.S. Tsai and M.-R. Wu, *Probing cosmic-ray accelerated light dark matter with IceCube*, *JCAP* **10** (2020) 049 [arXiv:2004.03161] [INSPIRE].

[27] S.-F. Ge, J. Liu, Q. Yuan and N. Zhou, *Diurnal effect of sub-GeV dark matter boosted by cosmic rays*, *Phys. Rev. Lett.* **126** (2021) 091804 [arXiv:2005.09480] [INSPIRE].

[28] G. Guo, Y.-L.S. Tsai, M.-R. Wu and Q. Yuan, *Elastic and inelastic scattering of cosmic-rays on sub-GeV dark matter*, *Phys. Rev. D* **102** (2020) 103004 [arXiv:2008.12137] [INSPIRE].

[29] N.F. Bell et al., *Cosmic-ray upscattered inelastic dark matter*, *Phys. Rev. D* **104** (2021) 076020 [arXiv:2108.00583] [INSPIRE].

[30] P. Gallagher, S. Groote and M. Naeem, *Gauge dependence of the gauge boson projector*, *Particles* **3** (2020) 543 [arXiv:2001.04106] [INSPIRE].

[31] M.A. Ivanov, J.G. Körner and C.T. Tran, *Exclusive decays* $B \to \ell^- \bar{\nu}$ *and* $B \to D^{(*)}\ell^- \bar{\nu}$ *in the covariant quark model*, *Phys. Rev. D* **92** (2015) 114022 [arXiv:1508.02678] [INSPIRE].

[32] H. Ruegg and M. Ruiz-Altaba, *The Stueckelberg field*, *Int. J. Mod. Phys. A* **19** (2004) 3265 [hep-th/0304245] [INSPIRE].

[33] Z. Liu, Y. Su, Y.-L. Sming Tsai, B. Yu and Q. Yuan, *A combined analysis of PandaX, LUX, and XENON*1*T experiments within the framework of dark matter effective theory*, *JHEP* **11** (2017) 024 [arXiv:1708.04630] [INSPIRE].

[34] J.D. Lewin and P.F. Smith, *Review of mathematics, numerical factors, and corrections for dark matter experiments based on elastic nuclear recoil*, *Astropart. Phys.* **6** (1996) 87 [INSPIRE].

[35] Y. Huang et al., *The Milky Way's rotation curve out to* 100 *kpc and its constraint on the galactic mass distribution*, *Mon. Not. Roy. Astron. Soc.* **463** (2016) 2623 [arXiv:1604.01216].

[36] XENON collaboration, *First dark matter search results from the XENON*1*T experiment*, *Phys. Rev. Lett.* **119** (2017) 181301 [arXiv:1705.06655] [INSPIRE].

[37] A.W. Strong and I.V. Moskalenko, *Propagation of cosmic-ray nucleons in the galaxy*, *Astrophys. J.* **509** (1998) 212 [astro-ph/9807150] [INSPIRE].

[38] M.J. Boschini et al., *Solution of heliospheric propagation: unveiling the local interstellar spectra of cosmic ray species*, *Astrophys. J.* **840** (2017) 115 [arXiv:1704.06337] [INSPIRE].

[39] PARTICLE DATA GROUP collaboration, *Review of particle physics*, *PTEP* **2020** (2020) 083C01 [INSPIRE].

[40] K. Bondarenko, A. Boyarsky, T. Bringmann, M. Hufnagel, K. Schmidt-Hoberg and A. Sokolenko, *Direct detection and complementary constraints for sub-GeV dark matter*, *JHEP* **03** (2020) 118 [arXiv:1909.08632] [INSPIRE].

[41] A.L. Fitzpatrick, W. Haxton, E. Katz, N. Lubbers and Y. Xu, *The effective field theory of dark matter direct detection*, *JCAP* **02** (2013) 004 [arXiv:1203.3542] [INSPIRE].

[42] A.L. Fitzpatrick, W. Haxton, E. Katz, N. Lubbers and Y. Xu, *Model independent direct detection analyses*, arXiv:1211.2818 [INSPIRE].

[43] N. Anand, A.L. Fitzpatrick and W.C. Haxton, *Weakly interacting massive particle-nucleus elastic scattering response*, *Phys. Rev. C* **89** (2014) 065501 [arXiv:1308.6288] [INSPIRE].

[44] F. Bishara, J. Brod, B. Grinstein and J. Zupan, *Chiral effective theory of dark matter direct detection*, *JCAP* **02** (2017) 009 [arXiv:1611.00368] [INSPIRE].

[45] F. Bishara, J. Brod, B. Grinstein and J. Zupan, *DirectDM: a tool for dark matter direct detection*, arXiv:1708.02678 [INSPIRE].

[46] J. Liu, *First results from PandaX-4T*, https://indico.icranet.org/event/1/contributions/37/attachments/310/378/PandaX-4T-1st-release-MG16-7-8-2021.pdf.

[47] R. Barbieri and T.E.O. Ericson, *Evidence against the existence of a low mass scalar boson from neutron-nucleus scattering*, *Phys. Lett. B* **57** (1975) 270 [INSPIRE].

[48] H. Leeb and J. Schmiedmayer, *Constraint on hypothetical light interacting bosons from low-energy neutron experiments*, *Phys. Rev. Lett.* **68** (1992) 1472 [INSPIRE].

[49] E. Izaguirre, G. Krnjaic and B. Shuve, *Discovering inelastic thermal-relic dark matter at colliders*, *Phys. Rev. D* **93** (2016) 063523 [arXiv:1508.03050] [INSPIRE].

[50] A. Berlin and F. Kling, *Inelastic dark matter at the LHC lifetime frontier: ATLAS, CMS, LHCb, CODEX-b, FASER, and MATHUSLA*, *Phys. Rev. D* **99** (2019) 015021 [arXiv:1810.01879] [INSPIRE].

[51] D.W. Kang, P. Ko and C.-T. Lu, *Exploring properties of long-lived particles in inelastic dark matter models at Belle II*, *JHEP* **04** (2021) 269 [arXiv:2101.02503] [INSPIRE].

[52] A. Aranda and C.D. Carone, *Limits on a light leptophobic gauge boson*, *Phys. Lett. B* **443** (1998) 352 [hep-ph/9809522] [INSPIRE].

[53] S. Tulin, *New weakly-coupled forces hidden in low-energy QCD*, *Phys. Rev. D* **89** (2014) 114008 [arXiv:1404.4370] [INSPIRE].

[54] C.-Y. Chen, D. McKeen and M. Pospelov, *New physics via pion capture and simple nuclear reactions*, *Phys. Rev. D* **100** (2019) 095008 [arXiv:1905.12017] [INSPIRE].

[55] A.M. Suliga, S. Shalgar and G.M. Fuller, *A closer look at the pp-chain reaction in the sun: constraining the coupling of light mediators to protons*, *JCAP* **07** (2021) 042 [arXiv:2012.11620] [INSPIRE].

[56] X.-W. Kang and J.A. Oller, *Different pole structures in line shapes of the* $X(3872)$, *Eur. Phys. J. C* **77** (2017) 399 [arXiv:1612.08420] [INSPIRE].

[57] X.-W. Kang, B. Kubis, C. Hanhart and U.-G. Meißner, B_{l4} *decays and the extraction of* $|V_{ub}|$, *Phys. Rev. D* **89** (2014) 053015 [arXiv:1312.1193] [INSPIRE].

[58] L. Zhang, X.-W. Kang, X.-H. Guo, L.-Y. Dai, T. Luo and C. Wang, *A comprehensive study on the semileptonic decay of heavy flavor mesons*, *JHEP* **02** (2021) 179 [arXiv:2012.04417] [INSPIRE].

[59] XENON100 collaboration, *Implications on inelastic dark matter from* 100 *live days of XENON*100 *data*, *Phys. Rev. D* **84** (2011) 061101 [arXiv:1104.3121] [INSPIRE].

[60] K. Schmidt-Hoberg and M.W. Winkler, *Improved constraints on inelastic dark matter*, *JCAP* **09** (2009) 010 [arXiv:0907.3940] [INSPIRE].

[61] S. Chang, G.D. Kribs, D. Tucker-Smith and N. Weiner, *Inelastic dark matter in light of DAMA/LIBRA*, *Phys. Rev. D* **79** (2009) 043513 [arXiv:0807.2250] [INSPIRE].